The Astrophysical Journal, 974:310 (23pp), 2024 October 20 https://doi.org/10.3847/1538-4357/ad6ddb

Hydrodynamics and Nucleosynthesis of Jet-driven Supernovae. II. Comparisons with Abundances of Extremely Metal-poor Galaxies and Constraints on Supernova Progenitors

Shing-Chi Leung[1] and Ken'ichi Nomoto[2]
[1] Department of Mathematics and Physics, SUNY Polytechnic Institute, 100 Seymour Road, Utica, NY 13502, USA; leungs@sunypoly.edu
[2] Kavli Institute for the Physics and Mathematics of the Universe (WPI), The University of Tokyo Institutes for Advanced Study, The University of Tokyo, Kashiwa, Chiba 277-8583, Japan
Received 2023 December 21; revised 2024 August 3; accepted 2024 August 8; published 2024 October 18

Abstract

The spectra of several galaxies, including extremely metal-poor galaxies from EMPRESS, have shown that the abundances of some Si-group elements differ from "spherical" explosion models of massive stars. This leads to the speculation that these galaxies have experienced supernova explosions with high asphericity, where mixing and fallback of the inner ejecta with the outer material lead to the distinctive chemical compositions. In this paper, we consider the jet-driven supernova models by direct 2D hydrodynamics simulations using progenitors of about 20–25 $M_\odot$ at zero metallicity. We investigate how the abundance patterns depend on the progenitor mass, mass cut, and asphericity of the explosion. We compare the observable with available supernova and galaxy catalogs based on ^{56}Ni, ejecta mass, and individual element ratios. The proximity of our results with the observational data signifies the importance of aspherical supernova explosions in chemical evolution of these galaxies. Our models will provide the theoretical counterpart for understanding the chemical abundances of high-z galaxies measured by the James Webb Space Telescope.

Unified Astronomy Thesaurus concepts: Supernovae (1668); Hypernovae (775); Hydrodynamical simulations (767); Relativistic jets (1390); Explosive nucleosynthesis (503); Chemical abundances (224)

1. Introduction

1.1. Aspherical Supernova Explosion

Many observable features of core-collapse supernovae (CCSNe) suggest that the their explosion could be aspherical. The clumpiness, filament structures, and observed directional variations of the ejecta imply aspherical explosion histories. This is further supported by evidence, including (1) the ring-shape structure of SN 1987A (L. Wang & P. A. Mazzali 1992) and the clear bipolar motion of high-speed knots in opposite directions (R. A. Fesen 2001), (2) the level of polarization in SN 1993J (H. D. Tran et al. 1997) and SN 1998bw (P. Höflich et al. 1999; L. Dessart et al. 2017), (3) the high-speed radioactive "bullets" in the Vela SN remnant (R. Strom et al. 1995), and (4) the high-velocity compact remnants discovered in the Vela SN (R. Strom et al. 1995).

The aspherical explosion can result from standard CCSNe by neutrino-driven explosions through the standing accretion shock instability (T. Foglizzo et al. 2015). The recent modeling approaches and results are reviewed in H.-T. Janka et al. (2016), A. Burrows & D. Vartanyan (2021), and B. Müller (2020). However, the actual explosion is subject to the intricate input physics, such as the equations of state, the neutrino physics, and the progenitors (e.g., A. Burrows et al. 2018). Variations such as the magnetorotational explosion and the outburst from the black hole accretion disk (i.e., jet-driven explosion or collapsar) are also possible candidates for explaining aspherical explosions.

Simulations of jet-driven explosions from an accretion disk wind were first suggested by A. M. Khokhlov et al. (1999). How the jet propagates through the stellar envelope is studied extensively in, e.g., A. I. MacFadyen et al. (2001). The models are applied to explain the polarimetric observations of some Type II SNe (S. M. Couch et al. 2009) and some shock-breakout light curves such as SN 2008D (S. M. Couch et al. 2011).

The magnetorotational instability (e.g., J. M. LeBlanc & J. R. Wilson 1970; M. Obergaulinger et al. 2009; M. Obergaulinger & M. Reichert 2023; B. Müller 2024) is required for a jet-like structure to develop outside a neutron star. But recent 3D simulations suggested that the collimation could be limited by kink instabilities (P. Mösta et al. 2014; T. Kuroda et al. 2020). In a similar background, the magnetic field can power the jet from the black hole accretion disk (S.-i. Fujimoto et al. 2006). Similarly, the neutrino also affects the disk dynamics and its nucleosynthesis (R. Surman & G. C. McLaughlin 2004). In both cases, the rotation is key for the accretion disk to grow, which can lead to a jet outburst that supplies a tremendous amount of energy ($\sim 10^{51}$ erg) to the envelope. The rotation model is particularly important because massive stars with a mass $\geqslant 18\,M_\odot$ might explode as hypernovae[3] to explain the bifurcation of explosion events (K. Nomoto et al. 2003).

For rotating models, how fast the star rotates depends on the angular momentum loss, which is hinged on the stellar mass loss. In metal-poor stars, the lack of metals for line absorption suppresses the stellar mass-loss rate and a massive H envelope persists (e.g., P. Marigo et al. 2001; H. Song et al. 2020;

[3] We remind that the term "hypernova" is used in the spherical explosion models, which require more than 10 times higher explosion energies than normal bright SNe. It outlines the difference for SN models with or without gamma-ray bursts (K. Iwamoto et al. 1998).

S. Martinet et al. 2023). Depending on the transfer of angular momentum from the core to the envelope, the core is suggested to obtain a high rotation velocity (L. J. Murphy et al. 2021), which favors the aspherical explosions. Some rotating first-star models studied in S. Ekström et al. (2008) show Fe cores capable of forming maximally rotating black holes. These black holes will be a potential site for the later jet outburst.

Once the jet forms, the cone-shaped energy deposition creates a very different thermodynamical history from a spherical explosion. This creates enhanced production around $A = 45$ and 65 (e.g., S. Nagataki et al. 1997). The high temperature creates the alpha-rich freeze-out, which is essential for producing individual isotopes such as ^{44}Ca, $^{47-48}$Ti, and ^{59}Co (e.g., K. Maeda et al. 2002). Similar results are observed for the zero-metallicity star explosion performed in N. Tominaga (2009). The jet energy deposition triggers aspherical mass ejection, which can explain the carbon-enhanced metal-poor (CEMP) stars (N. Tominaga et al. 2007a) and some Zn-rich stars such as HE 1327-2326 (R. Ezzeddine et al. 2019). The jet structure also favors the ejection of ^{56}Ni-rich matter with a high velocity (S. Nagataki et al. 1998; P. A. Mazzali et al. 2005; K. Maeda et al. 2006), which has been observed in some SNe and hypernovae (e.g., SN 1987A, SN 1998bw). The energy composition of the jet also leaves a signature by the polarization of the ejecta (e.g., S. M. Couch et al. 2009).

1.2. Spectroscopic Observations

The search for high-redshift galaxies has opened another dimension in understanding the nature of SN explosions, especially low-metallicity ones. Similar to extremely metal-poor (EMP) stars, EMP galaxies are ideal candidates to capture the effects of early massive SN explosion by their chemical composition, which reflects the explosive yield of one or a few SN explosions (e.g., T. Hartwig et al. 2018). Such early galaxies also imply that the Type Ia SNe are less important, which have a delay time from the formation of white dwarfs to their final explosions (e.g., C. Kobayashi et al. 2020). Thus, the composition of these extreme metal-poor objects provides direct constraints on the massive-star explosion yields. Recent surveys, as well as their follow-up observations, have discovered several galactic objects with unusual Si- and Fe-group elements, including Ne, Si, S, Ar, Fe, and Ni.

In T. Kojima et al. (2020) the Extremely Metal-Poor Representatives Explored by the Subaru Survey (EMPRESS) is designed to use the Subaru/Hyper Supreme-Cam optical images to identify the faint EMP galaxies. Among the >100 EMP galaxies identified, their follow-up project later selected 13 galaxies and studied them in detail, where the galaxies have a metallicity $Z \sim 0.1\% - 1\% Z_{\odot}$ (Y. Isobe et al. 2022). They measured the α-chain elements O, Ne, Ar, and Fe, which can be directly connected to the massive-star progenitors and explosion mechanisms. Among all features, these galaxies have [Ne/O], [Ar/O], and [Fe/O] values very close to solar values or mildly subsolar, despite their high metal-poor nature.

In K. Watanabe et al. (2024), the 13th follow-up project on the analysis of the galaxy catalog from the EMPRESS project is reported for more EMP galaxies, including SBS-0335-052E (Y. I. Izotov et al. 2018), J2314+0154 (T. Kojima et al. 2020), and J0125+0759 (T. Kojima et al. 2020). The spectra of these galaxies are measured by Keck/LRIS. Ratios of [Ne/O], [Ar/O], [S/O], and [Fe/O] are reported. In that work, the mixing–fallback model is extensively adopted to explain the unconventional abundance pattern. These galaxies are shown to fit with a small mixing ratio, about 0–0.2; however, the [Fe/O] cannot be fully explained by the mixing and fallback mechanisms. [Ar/O] and [S/O] could be indicators of PISN explosions.

1.3. Motivation

The chemical abundances provide firsthand constraints on how massive stars explode and eject matter to the surroundings (e.g., F.-K. Thielemann 2019; A. Arcones & F.-K. Thielemann 2023). The discrepancies between the measured galaxies' chemical abundance and nucleosynthesis yields of ordinary stars have led to comparisons with less canonical SN models, including hypernovae and pair-instability SN (PISN) models (Y. Isobe et al. 2022). While the early galaxies favor the formation of very massive stars (e.g., S. Hirano et al. 2015), later radiation hydrodynamics simulations suggest ordinary massive stars (see, e.g., M. A. Latif et al. 2022). This implies that both ordinary and very massive stars are possible candidates for the chemical origin of these galaxies. The mismatch of chemical abundances of these galaxies with nucleosynthesis yields of spherical models leads to the question whether other models can explain the abundance pattern. For example, very massive stars (T. E. Woods et al. 2020; H. Umeda & C. Nagele 2024) are often invoked for matching less commonly seen nucleosynthetic patterns.

In 1D simulations, the mixing–fallback model has been invoked to mimic the multidimensional mixing process (H. Umeda & K. Nomoto 2002). The mixing–fallback approximation has successfully explained the peculiar abundance patterns of some metal-poor stars, such as the very high C/Fe abundance ratio (e.g., H. Umeda & K. Nomoto 2002; M. N. Ishigaki et al. 2018). The mixing processes have been shown in neutrino-driven explosions as exhibited by their highly aspherical structure (see characteristic simulations from various groups, e.g., A. Burrows et al. 2012; E. J. Lentz et al. 2015; T. Melson et al. 2015).

In Paper I (S.-C. Leung et al. 2023) we presented a catalog of the jet-driven SN models using multidimensional simulations. The model uses a 40 $M_{\odot}$ zero-metallicity Population III star as the progenitor. The jet-like thermal bomb is applied to parameterize the explosion process in the center. We studied nucleosynthesis of the jet-triggered explosion and showed how the chemical composition depends on the jet energetics. The yields of the jet models exhibit significant differences from spherical explosion models. The jet explosion is essential in reproducing the trend of some element pair such as Ti and V. It is therefore interesting to extend our models and check whether the results derived from a more consistent modeling provide better fitting.

In this paper, we first review the essential massive-star models presented in this work in Section 2. We describe how the massive-star explosion models are prepared in both one and two dimensions. Then, in Section 3 we present how the hydrodynamics and nucleosynthesis depend on the dimensionality, progenitor mass, and other input physics. In Section 4 we analyze the elemental trends of some key element pairs and compare them with the observed metal-poor stars and SNe. We also present the elemental yields of our models. We apply our results to compare with some well-observed metal-poor galaxies and some metal-poor stars in Section 5. Finally, we give our conclusion in Section 6.

Table 1
The Jet-driven Supernova Models Using the 20 $M_\odot$ ZAMS Star for the Progenitor

Model	$M_{\rm ZAMS}$	$M_{\rm pro}$	$\dot{E}_{\rm dep}$	$t_{\rm dep}$	$E_{\rm dep}$	$\theta_{\rm jet}$	$M_{\rm ej}$	M(O)	[Ne/O]	[Si/O]	[S/O]	[Ar/O]	[Fe/O]
S20-0250-1000-15	20	4.08	0.25	1.00	0.375	15	1.94	1.02	0.14	−1.01	−1.08	−1.17	−0.70
S20-0500-0500-15	20	4.08	0.50	0.50	0.375	15	2.62	1.42	0.14	−0.80	−0.88	−0.97	−0.85
S20-0500-1000-15	20	4.08	0.50	1.00	0.750	15	2.81	1.53	0.14	−0.73	−0.77	−0.86	−0.79
S20-0500-2000-15	20	4.08	0.50	2.00	1.500	15	2.91	1.59	0.13	−0.71	−0.75	−0.83	−0.80
S20-1000-0500-15	20	4.08	1.00	0.50	0.750	15	3.17	1.58	0.13	−0.64	−0.66	−0.72	−0.83
S20-1000-0250-15	20	4.08	1.00	0.25	0.375	15	2.87	1.73	0.14	−0.82	−0.94	−1.05	−0.90
S20-1000-1000-15	20	4.08	1.00	1.00	1.500	15	3.18	1.76	0.13	−0.65	−0.68	−0.76	−1.05
S20-1000-2000-15	20	4.08	1.00	2.00	3.000	15	3.25	1.81	0.13	−0.60	−0.64	−0.71	−1.05
S20-1000-4000-15	20	4.08	1.00	4.00	6.000	15	3.34	1.78	0.13	−0.61	−0.63	−0.70	−0.84
S20-2000-0500-15	20	4.08	2.00	0.50	1.500	15	3.48	1.81	0.13	−0.52	−0.51	−0.57	−0.76
S20-2000-1000-15	20	4.08	2.00	1.00	3.000	15	3.46	1.91	0.12	−0.50	−0.51	−0.59	−0.87
S20-2000-2000-15	20	4.08	2.00	2.00	6.000	15	3.55	1.88	0.11	−0.40	−0.38	−0.43	−0.82
S20-4000-1000-15	20	4.08	4.00	1.00	6.000	15	3.59	1.94	0.12	−0.34	−0.32	−0.37	−0.74
S20-4000-2000-15	20	4.08	4.00	2.00	12.000	15	3.56	1.94	0.12	−0.40	−0.40	−0.47	−0.79

Note. $M_{\rm ZAMS}$, $M_{\rm pro}$, $M_{\rm ej}$, and M(O) are the progenitor ZAMS, pre-collapse, ejecta, and ejected O masses in units of $M_\odot$, respectively. $\dot{E}_{\rm dep}$, $t_{\rm dep}$, and $E_{\rm dep}$ are the energy deposition rate, deposition time, and total deposited energy in units of the characteristic model, respectively. [Ne/O], [Si/O], [S/O], [Ar/O], and [Fe/O] are the ejecta mass fraction ratios of the element pairs, defined in Equation (1). The model name SWW-XXXX-YYYY-ZZ stands for the model using ZAMS mass WW $M_\odot$, XXXX/1000 $\dot{E}_{\rm ref}$, YYYY/1000 $t_{\rm ref}$, and a ZZ° open angle. See also Table 10 for C–Zn of this model series.

This paper uses the convention

$$[\mathrm{X/Fe}] = \log_{10}\frac{(\mathrm{X/Fe})}{(\mathrm{X/Fe})_\odot}. \quad (1)$$

2. Massive-star Models

2.1. Two-dimensional Simulations

In Paper I (S.-C. Leung et al. 2023), we studied the dependence of explosive nucleosynthesis on the jet explosion parameters for the 40 $M_\odot$ star progenitor using the special relativistic hydrodynamics solver extended from S.-C. Leung et al. (2015). The jet energy deposition rate, its duration, and the open angles are treated as main parameters. We followed N. Tominaga (2009) and set the standard jet as $\dot{E}_{\rm dep,0} = 1.2 \times 10^{53}$ ergs^{-1}, $E_{\rm dep,0} = 1.5 \times 10^{52}$ erg, and a jet open angle of 15°. This implies a jet deposition time of $t_{\rm jet,0} = 0.125$ s.

In each model, we first remove the core material interior to the mass cut and then deposit the energy at the inner boundary of the jet with the jet prescription above. We adopt the Helmholtz equation of state (F. X. Timmes & D. Arnett 1999; F. X. Timmes & F. D. Swesty 2000) and a simple seven-isotope network (F. X. Timmes et al. 2000) to describe nuclear reactions in the hydrodynamics simulations. We calculate the explosion until most exothermic nuclear reactions have terminated and the ejecta appears to be in homologous expansion to a good approximation.

In the simulations, we use the tracer particle scheme (e.g., D. Arnett et al. 1989; I. Hachisu et al. 1990; C. Travaglio et al. 2004; I. R. Seitenzahl et al. 2010) to record the thermodynamic history of the underlying fluid motion. After the hydrodynamics simulations, we use the thermodynamic histories of the tracer particles to reconstruct the detailed nucleosynthesis with the 495-isotope network containing isotopes from H to Tc (F. X. Timmes 1999).

We extend our calculation to include progenitors with the zero-age main-sequence (ZAMS) masses of $M_{\rm ZAMS} = 20$ and 25 $M_\odot$ presented in N. Tominaga et al. (2007b). Recent pre-SN and core-collapse models (e.g., T. Sukhbold et al. 2016) have demonstrated the possibilities of the formation of an accretion disk and a following outburst. This also agrees with the suggestions by K. Nomoto et al. (2013) that the final fate of stars with $M_{\rm ZAMS} \geqslant 25\,M_\odot$ can bifurcate into faint SNe and hypernovae following fallback. In Tables 1–4 we list the new models computed in this work and some of their essential parameters. For convenience we name all the models in the following format: S20-0500-2000-15 corresponds to the progenitor model with $M_{\rm ZAMS} = 20\ M_\odot$ (S20), the jet with an energy deposition rate of $0.5\dot{E}_{\rm jet,0}$ (0500), a jet deposition time of $2.0t_{\rm jet,0}$ (2000), and an open angle of 15° (15). All models assume the inner boundary at 900 km, except for the series S25b (s25c), which corresponds to the model sequence where the innermost boundary is located at 1500 (2100) km. In Appendix A we further tabulate the elemental ratios of other major elements from these models.

In Figure 1 we plot the tracer distribution of the characteristic model using the 25 $M_\odot$ star progenitor. We use the final energy of the tracers to determine whether they are ejected or bound. The Si layer within the cone shape is ejected. The inner C+O layer has an increasing spread in the ejecta angular range until ∼20,000 km. Beyond that, the outer shell is ejected.

We summarize the tracer thermodynamic history in Figure 2. It collects the statistics of the passive tracers in the characteristic model when the tracers reach their maximum temperature. We bin the tracers according to their corresponding density. In Figure 2, the data points correspond to the average of the tracers within individual density bins, and the error bars stand for the standard deviation of the data.

The thermodynamics provides a useful diagnosis to the nuclear reaction class which the tracers have experienced. In general, high-density and high-temperature burning leads to nuclear statistical equilibrium (NSE), where the composition can be solely determined by ρ, T, and Y_e. In NSE, the final composition can be predicted by the density where the matter leaves NSE. On the other hand, for a low-density and high-temperature environment, α-burning becomes the bottleneck of the entire nuclear reaction network. Thus, not all isotopes are equally accessible as in NSE. This gives rise to a unique

Table 2
Same as Table 1, but for Models Using the 25 $M_\odot$ Progenitor as the Pre-collapse Model

Model	$M_{\rm ZAMS}$	$M_{\rm pro}$	$\dot{E}_{\rm dep}$	$t_{\rm dep}$	$E_{\rm dep}$	$\theta_{\rm jet}$	$M_{\rm ej}$	M(O)	[Ne/O]	[Si/O]	[S/O]	[Ar/O]	[Fe/O]
S25-0250-1000-15	25	5.58	0.25	1.00	0.375	15	1.76	0.64	−0.33	−0.11	−0.01	−0.06	−0.02
S25-0250-2000-15	25	5.58	0.25	2.00	0.750	15	1.51	0.61	−0.41	−0.06	0.02	−0.03	−0.89
S25-0500-0500-15	25	5.58	0.50	0.50	0.375	15	2.62	1.07	−0.30	−0.33	−0.26	−0.35	−0.29
S25-0500-1000-15	25	5.58	0.50	1.00	0.750	15	2.74	1.26	−0.35	−0.14	−0.07	−0.13	−0.19
S25-0500-2000-15	25	5.58	0.50	2.00	1.500	15	2.50	1.22	−0.36	−0.20	−0.14	−0.20	−0.57
S25-0500-4000-15	25	5.58	0.50	4.00	3.000	15	3.02	1.44	−0.34	−0.14	−0.08	−0.15	−0.20
S25-1000-0250-15	25	5.58	1.00	0.25	0.375	15	1.50	0.60	−0.33	−0.62	−0.60	−0.67	−0.41
S25-1000-0500-15	25	5.58	1.00	0.50	0.750	15	3.31	1.67	−0.31	−0.20	−0.16	−0.22	−0.31
S25-1000-1000-15	25	5.58	1.00	1.00	1.500	15	3.61	1.78	−0.33	−0.12	−0.08	−0.13	−0.20
S25-1000-1000-30	25	5.58	1.00	1.00	1.500	30	3.75	1.84	−0.37	−0.08	−0.05	−0.11	−0.11
S25-1000-2000-15	25	5.58	1.00	2.00	3.000	15	3.62	1.80	−0.32	−0.13	−0.09	−0.16	−0.19
S25-1000-2000-30	25	5.58	1.00	2.00	3.000	30	3.84	1.87	−0.37	−0.04	−0.01	−0.06	0.01
S25-1000-4000-15	25	5.58	1.00	4.00	6.000	15	3.20	1.74	−0.32	−0.26	−0.26	−0.34	−0.75
S25-2000-0250-15	25	5.58	2.00	0.25	0.750	15	3.63	1.84	−0.29	−0.27	−0.26	−0.32	−0.19
S25-2000-0500-15	25	5.58	2.00	0.50	1.500	15	3.97	1.99	−0.34	−0.12	−0.11	−0.17	−0.17
S25-2000-1000-15	25	5.58	2.00	1.00	3.000	15	4.00	2.04	−0.36	−0.11	−0.11	−0.18	−0.20
S25-2000-1000-30	25	5.58	2.00	1.00	3.000	30	4.12	2.02	−0.39	−0.03	−0.01	−0.07	−0.00
S25-2000-2000-15	25	5.58	2.00	2.00	6.000	15	4.02	2.09	−0.41	−0.08	−0.11	−0.19	−0.29
S25-2000-2000-30	25	5.58	2.00	2.00	6.000	30	4.23	2.01	−0.43	0.04	0.07	0.01	0.07
S25-4000-0500-15	25	5.58	4.00	0.50	3.000	15	4.33	2.17	−0.41	−0.01	−0.00	−0.06	−0.15
S25-4000-1000-15	25	5.58	4.00	1.00	6.000	15	4.29	2.14	−0.49	0.09	0.11	0.05	−0.19
S25-4000-2000-15	25	5.58	4.00	2.00	12.00	15	4.44	2.08	−0.36	−0.11	−0.15	−0.23	−0.14

Note. See also Table 11 for C–Zn of this model series.

Table 3
Same as Table 2, but with an Innermost Boundary at 1500 km

Model	$M_{\rm ZAMS}$	$M_{\rm pro}$	$\dot{E}_{\rm dep}$	$t_{\rm dep}$	$E_{\rm dep}$	$\theta_{\rm jet}$	$M_{\rm ej}$	M(O)	[Ne/O]	[Si/O]	[S/O]	[Ar/O]	[Fe/O]
S25b-0500-1000-15	25	5.34	0.50	1.00	0.750	15	1.55	0.61	−0.33	−0.13	−0.04	−0.10	−0.14
S25b-0500-2000-15	25	5.34	0.50	2.00	1.500	15	1.41	0.60	−0.37	−0.22	−0.12	−0.16	−0.67
S25b-1000-0500-15	25	5.34	1.00	0.50	0.750	15	2.06	1.00	−0.35	−0.22	−0.15	−0.20	−0.50
S25b-1000-1000-15	25	5.34	1.00	1.00	1.500	15	2.37	1.14	−0.34	−0.18	−0.12	−0.17	−0.29
S25b-1000-2000-15	25	5.34	1.00	2.00	3.000	15	2.46	1.19	−0.34	−0.15	−0.10	−0.16	−0.26
S25b-1000-4000-15	25	5.34	1.00	4.00	6.000	15	2.48	1.34	−0.36	−0.24	−0.25	−0.33	−0.76
S25b-2000-0500-15	25	5.34	2.00	0.50	1.500	15	2.83	1.43	−0.33	−0.16	−0.13	−0.19	−0.30
S25b-2000-1000-15	25	5.34	2.00	1.00	3.000	15	2.91	1.47	−0.35	−0.12	−0.10	−0.16	−0.29
S25b-2000-2000-15	25	5.34	2.00	2.00	6.000	15	2.92	1.49	−0.36	−0.13	−0.14	−0.21	−0.28
S25b-4000-1000-15	25	5.34	4.00	1.00	6.000	15	3.03	1.59	−0.40	−0.00	0.03	−0.03	−0.39
S25b-4000-2000-15	25	5.34	4.00	2.00	12.000	15	3.06	1.58	−0.47	0.10	0.14	0.08	−0.42

Note. See also Table 12 for C–Zn of this model series.

Table 4
Same as Table 2, but with an Innermost Boundary at 2100 km

Model	$M_{\rm ZAMS}$	$M_{\rm pro}$	$\dot{E}_{\rm dep}$	$t_{\rm dep}$	$E_{\rm dep}$	$\theta_{\rm jet}$	$M_{\rm ej}$	M(O)	[Ne/O]	[Si/O]	[S/O]	[Ar/O]	[Fe/O]
S25c-0500-1000-15	25	5.21	0.50	1.00	0.750	15	1.48	0.52	−0.29	−0.31	−0.25	−0.32	−0.13
S25c-0500-2000-15	25	5.21	0.50	2.00	1.500	15	2.00	0.77	−0.33	−0.14	−0.05	−0.12	−0.35
S25c-1000-0500-15	25	5.21	1.00	0.50	0.750	15	2.05	0.78	−0.34	−0.21	−0.13	−0.18	−0.23
S25c-1000-1000-15	25	5.21	1.00	1.00	1.500	15	2.34	0.98	−0.33	−0.21	−0.14	−0.20	−0.36
S25c-1000-2000-15	25	5.21	1.00	2.00	3.000	15	2.90	1.41	−0.34	−0.23	−0.19	−0.27	−0.59
S25c-1000-4000-15	25	5.21	1.00	4.00	6.000	15	3.40	1.78	−0.35	−0.22	−0.21	−0.28	−0.74
S25c-2000-0500-15	25	5.21	2.00	0.50	1.500	15	3.15	1.52	−0.33	−0.19	−0.14	−0.21	−0.40
S25c-2000-1000-15	25	5.21	2.00	1.00	3.000	15	3.63	1.83	−0.32	−0.16	−0.12	−0.18	−0.45
S25c-2000-2000-15	25	5.21	2.00	2.00	6.000	15	4.00	2.06	−0.37	−0.08	−0.07	−0.15	−0.42
S25c-4000-1000-15	25	5.21	4.00	1.00	6.000	15	3.83	2.06	−0.35	−0.12	−0.10	−0.16	−0.70
S25c-4000-2000-15	25	5.21	4.00	2.00	12.000	15	4.02	2.11	−0.43	0.01	0.02	−0.05	−0.48

Note. See also Table 13 for C–Zn of this model series.

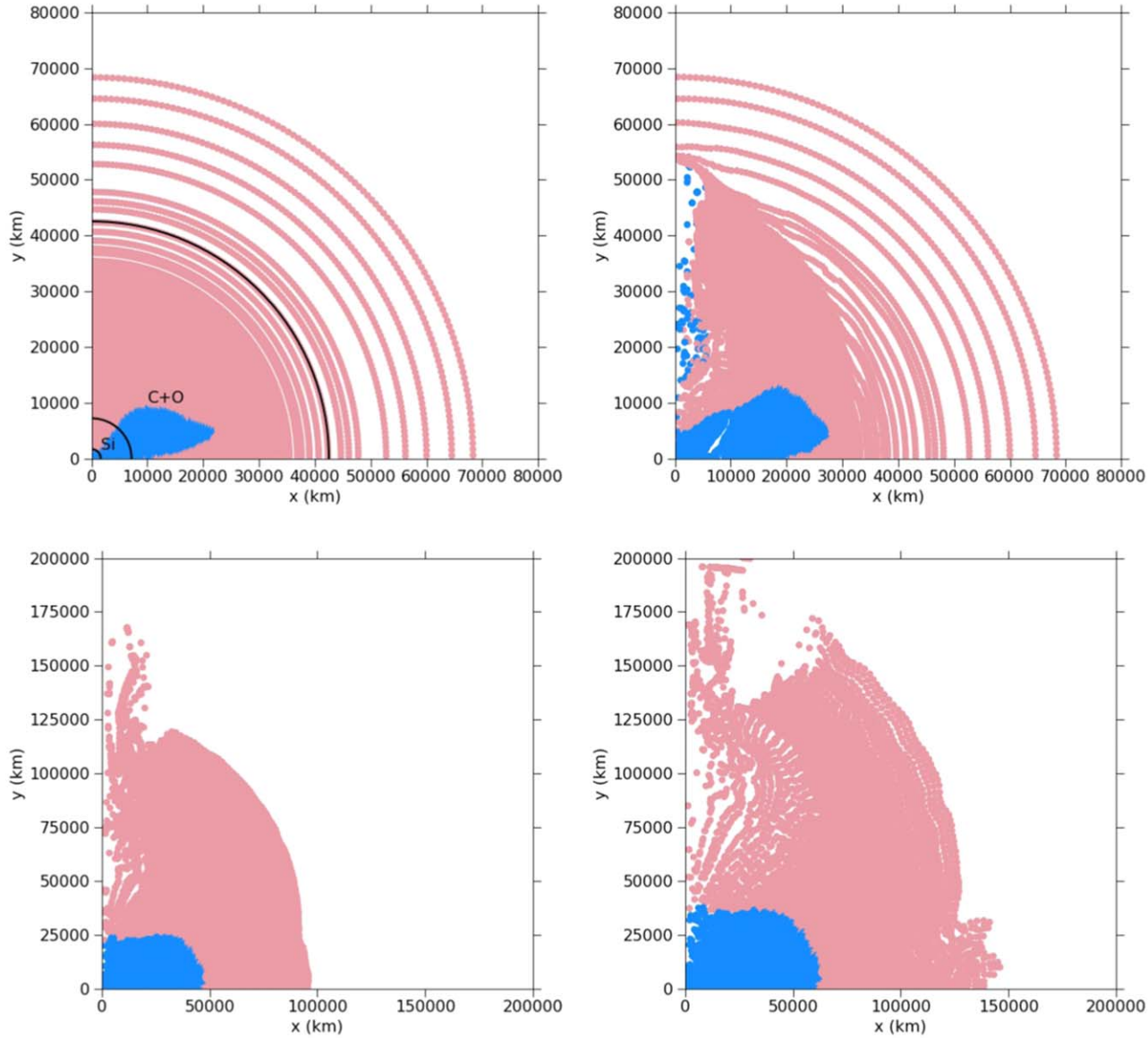

Figure 1. The tracer distribution in the characteristic 25 $M_{\odot}$ model, with red being ejected and blue being bound. The Si and C+O cores are indicated by the solid line for illustration. The top left, top right, bottom left, and bottom right panels stand for four snapshots at equal time steps of ∼4 s, starting from the initial profile.

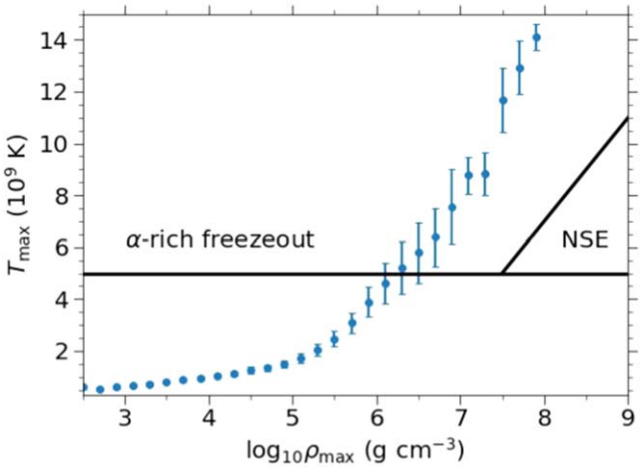

Figure 2. Statistics of the tracers for the peak temperature T_{max} and their corresponding density in the characteristic model S25-1000-1000-15.

chemical abundance pattern featuring high-entropy isotopes, e.g., ^{64}Zn.

In the characteristic model of the 25 $M_{\odot}$ star, we observe an almost monotonically increasing trend for the tracers. Tracers in the inner part of the star, having higher densities, experienced higher peak temperatures in their burning history. There are observable fluctuations for tracers from the inner ejecta. This is because the ejecta includes both the region directly excited by the jet and the nearby region that follows the expansion. Matter in the outer region is mostly ejected without experiencing a significant shock heating. The spherical-like mass ejection agrees with the low fluctuations among tracers.

In Figure 3 we plot the characteristic model using the 25 $M_{\odot}$ progenitor. The 2D model shows a flat distribution of chemical elements from C to Zn. Most elements along the α-chain have abundances compatible with the solar abundance. Odd-number elements such as P, K, Sc, and the low-Ye isotopes (i.e., the isotopes with a higher neutron number) are mostly under-produced. The zero-metallicity environment does not contain

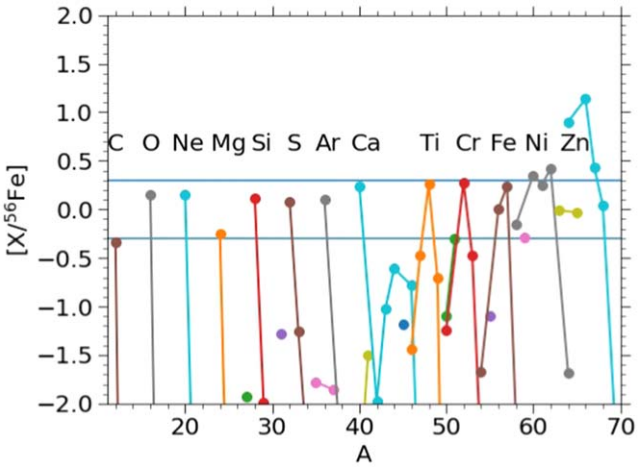

Figure 3. The scaled isotope fraction ($[X/Fe] = \log_{10}(X/Fe)/(X/Fe)_{\odot}$) for elements from C to Zn. The two horizontal lines stand for 50% and 200% of the solar value.

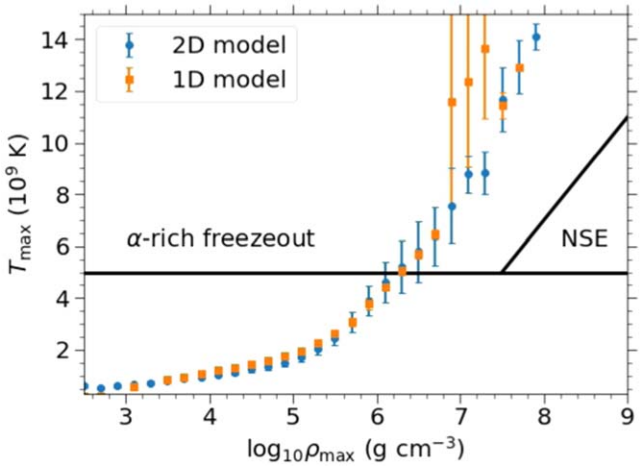

Figure 4. The tracer thermodynamics history for the 25 $M_{\odot}$ star assuming spherical (1D; orange squares) and jet-powered (2D; blue circles) explosions.

any ^{22}Ne to directly produce the low-Ye isotopes, especially in the Si-group elements.

2.2. Mixing–Fallback Mechanisms

The mixing–fallback model (H. Umeda & K. Nomoto 2002) is an approximate modeling of the jetlike aspherical mass ejection by using the spherical explosion model. The mixing–fallback model can reproduce the abundance pattern of the jetlike explosion rather well (N. Tominaga 2009). The model considered the process that, instead of the ejection of the entire star, a part of the inner core and outer envelope are mixed and ejected, and the remaining matter falls back and accretes onto the central compact object. The model assumes three parameters: (1) the inner mass cut $M_{\rm cut,\ in}$, (2) the outer mass cut $M_{\rm cut,\ out}$, and (3) the mixing ratio $f_{\rm mix}$. The mass interior to the inner mass cut all accretes. The total accreted mass is given by

$$M_{\rm acc} = M_{\rm cut,in} + (1 - f_{\rm mix})(M_{\rm cut,out} - M_{\rm cut,in}). \quad (2)$$

The exact mass of individual elements then depends on the composition of both the middle layer and the outer layer. This model has been used extensively to describe the origin of the peculiar chemical abundance patterns in EMP stars (e.g., N. Iwamoto et al. 2005; M. N. Ishigaki et al. 2018).

The mixing–fallback model can reproduce the abundance pattern of jetlike explosion rather well (N. Tominaga 2009). However, the spherical model is different from a full 2D or 3D model. Assuming an explosion of the same energy, the energy is deposited in a spherical shell, rather than being focused on the cone-shaped structure. Thus, the mixing–fallback model has (1) a less active nucleosynthesis and (2) a lower ejecta velocity. In Appendix B, we tabulate the stable and short-lived radioactive isotopes of the spherical models with various masses and explosion energy, together with their elemental production.

3. Explosive Observable and Nucleosynthesis

3.1. Dependence on Dimensionality

The most important effect of the jet-driven explosion on SN models is that the jet provides local heating for the matter to expand and to be ejected. This cannot be achieved in classical spherical models. In the aspherical model compared with the spherical model, a small explosion energy is enough for the ejecta to reach such high velocities as observed in some hypernovae or highly aspherical SNe (e.g., SN 1998bw studied in P. Höflich et al. 1999; P. A. Mazzali et al. 2001; T. Nakamura et al. 2001). This allows the aspherical model to synthesize and eject Fe-group elements more readily than the spherical model with the same explosion energy. Here we examine how the dimensionality changes nucleosynthetic products.

In Figure 4 we plot the tracer thermodynamics for the jet-driven SN model using the 25 $M_{\odot}$ star as the progenitor, and we compare with the spherical explosion model. The difference in the heating history is clear on the tracer particles: (1) In the 1D model, there are large variations in the temperature in the inner core with $\rho_{\rm max} > 10^7$ g cm^{-3}. However, there are very small or even no variations for tracers below that density. This is because the shock in the spherical model has lost most of its compressional heating effect at $\rho_{\rm max} < 10^7$ g cm^{-3}. (2) On the other hand, the angular effects remain clearly visible for the 2D model down to 10^5 g cm^{-3}. This suggests that the energy confined within 15°–30° helps the shock to maintain its strength to a larger spatial extension.

In Figure 5 we plot the abundance patterns of our characteristic models using 20, 25, and 40 $M_{\odot}$ progenitors, in comparison with the corresponding spherical (1D) models. Both sequences of models assume the same explosion energy $\sim 1.5 \times 10^{51}$ erg.

The progenitor mass also affects how the 2D and 1D models differ from each other. For the lower-mass model (20 $M_{\odot}$), the 2D explosion leads to the prominent overproduction of O- and Si-group elements along the α-chain, ^{16}O, ^{20}Ne, and ^{24}Mg. This can be understood by the entire ejection of the outer layers. The odd-number Si-group elements are underproduced in both models, with the exception that Ti and Cr are well produced in 1D models. The Fe-group elements in both models are similar to the solar ratio, while Ni is significantly overproduced in the 1D model. Zn is also overproduced in the 1D model but is substantially underproduced in the 2D model.

The 25 $M_{\odot}$ model is like a mixture of the 20 and 40 $M_{\odot}$ models. The O-group elements are weaker for the 1D model, while the Si-group elements are stronger. The chemical abundances from Si to Fe are very close to the solar

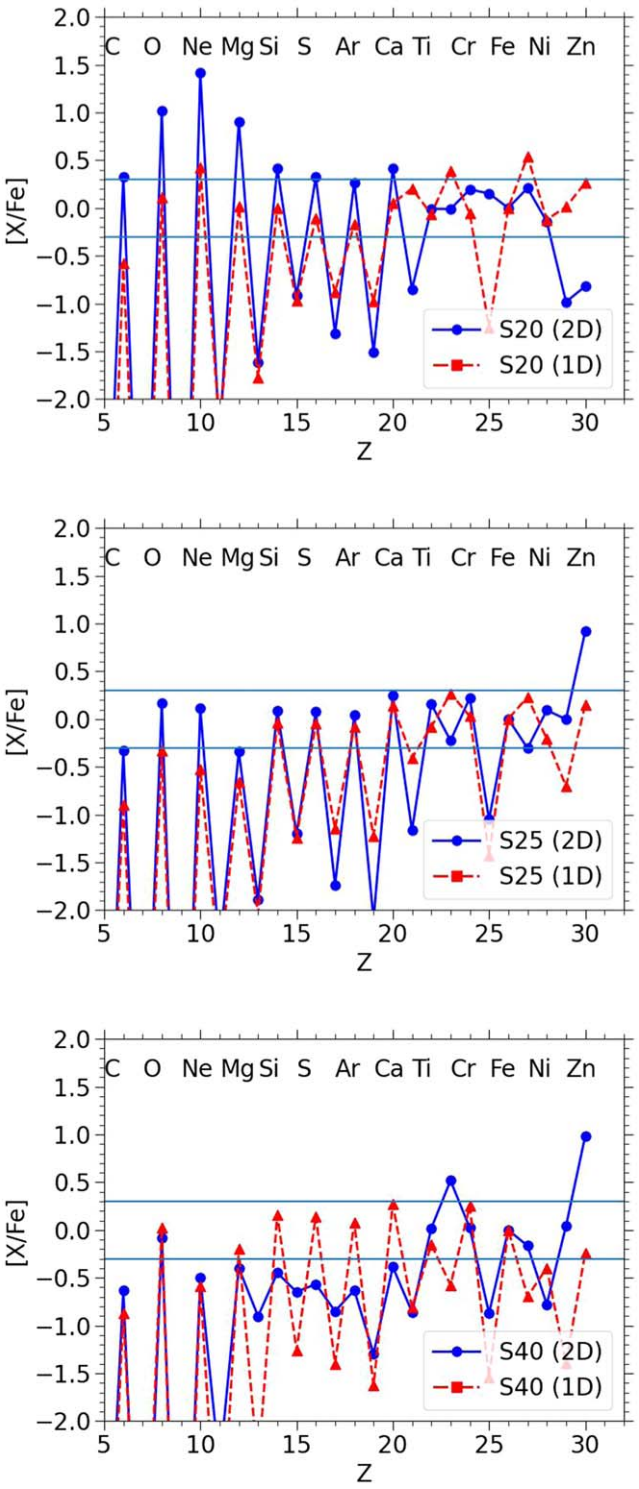

Figure 5. Top panel: the chemical abundances of Model S20-1000-1000-15 (blue solid line) and its 1D counterpart (red dashed line). Middle panel: same as the top panel, but for Model S25-1000-1000-15 and its 1D counterpart. Bottom panel: same as the top panel, but for Model S40-1000-1000-15 and its 1D counterpart.

abundances in both dimensionalities, with the exception of the odd-number elements. Ni is again overproduced in the spherical model. The overproduction suggests that, to reconcile with the solar abundance, the ejecta cannot contain the entire inner core of the star. The overproduction is less severe in the 2D model.

The 40 $M_\odot$ model is in sharp contrast with the 20 $M_\odot$ model. Most α-chain elements from Ne to Ti in the 2D model are underproduced, while the 1D model produces the amounts close to the solar values. The 2D model contains more weights in the Fe-group elements. The ejecta in the 2D model contains a clear Zn signature but a very low Ni abundance, where the 1D counterpart shows opposite trends. The parity of even-number charged elements versus odd-number charged elements (even–odd) is also smaller for the 2D model. The masses of even elements are similar in both models, but those of the odd elements are about 10 times higher in the 2D model. This is because in the 2D model the jet allows the fluid elements that produce Si-group elements ($\rho \sim 3 \times 10^5$ g cm^{-3} to 1×10^7 g cm^{-3}) to have a higher peak temperature when the shock arrives. In our 1D model the peak temperature reaches about 3.5×10^9 K, while in the 2D model it can reach about $(4\text{–}5) \times 10^9$ K. Such a high temperature strongly facilitates the production of odd elements.

To further visualize the effect of the mixing in one dimension and the 2D jet-driven explosions, we show in Figure 6 the 1D spherical model yields using the mixing–fallback mechanism, and we show in Figure 7 the 2D model sequences. In all 1D models, we choose the $E_{\rm exp} = 1 \times 10^{52}$ erg as the reference and vary the mixing parameter from 0 to 0.3 in 0.05 steps. This corresponds to the jet angle $\sim$45°. Different mixing masses are used from 3.0 to 6.0 $M_\odot$ for each model. We focus on the element pairs [Ne/O], [Ar/O], and [S/O] against [Fe/O], as these elements are frequently observed in galaxies.

The 1D spherical models in Figure 6 show vertical variations for different mixing ratios. We note the following: (1) [Ne/O] in 1D models is a good indicator of the progenitor mass for the following reason. Ne is synthesized by C burning, which produces larger X(Ne) from larger X(C) in the C+O core. The C/O ratio is smaller for the larger ^{12}C(α, γ)^{16}O reaction rate, which is higher for higher temperatures. Since the temperature in the C+O core is higher for the larger progenitor mass, the C/O ratio and thus the Ne/O ratio are smaller for a larger progenitor mass. The ratio does not depend on the mixing level or the mass cut.

(2) The [Fe/O] values of all spherical models are subsolar because the massive C+O layer is ejected, which strongly suppresses the ratio. This is in contrast to the 2D model, where a significant fraction of the O layer is accreted rather than ejected (see Figure 1). The subsolar patterns persist among all masses.

(3) For [Ar/O] and [S/O], there are two groups of models. When the mass cut is deep enough to completely isolate the Si core, these ratios against [Fe/O] appear to be slightly supersolar and vertical (right side of the plot). When the mass cut is moved outward, the ratios appear to align on a straight line. This is because the inner core also contains Ar and S.

The 2D models in Figure 7 show qualitatively different patterns from their 1D models except [Ne/O].

(1) [Ne/O] against [Fe/O] preserves its strong mass dependence as in the 1D models.

(2) Other two-element pairs show a large scatter. The [Fe/O] ratio is significantly higher than most 1D models. The 25 and 40 $M_\odot$ stars have much higher [Fe/O] than most 1D counterparts.

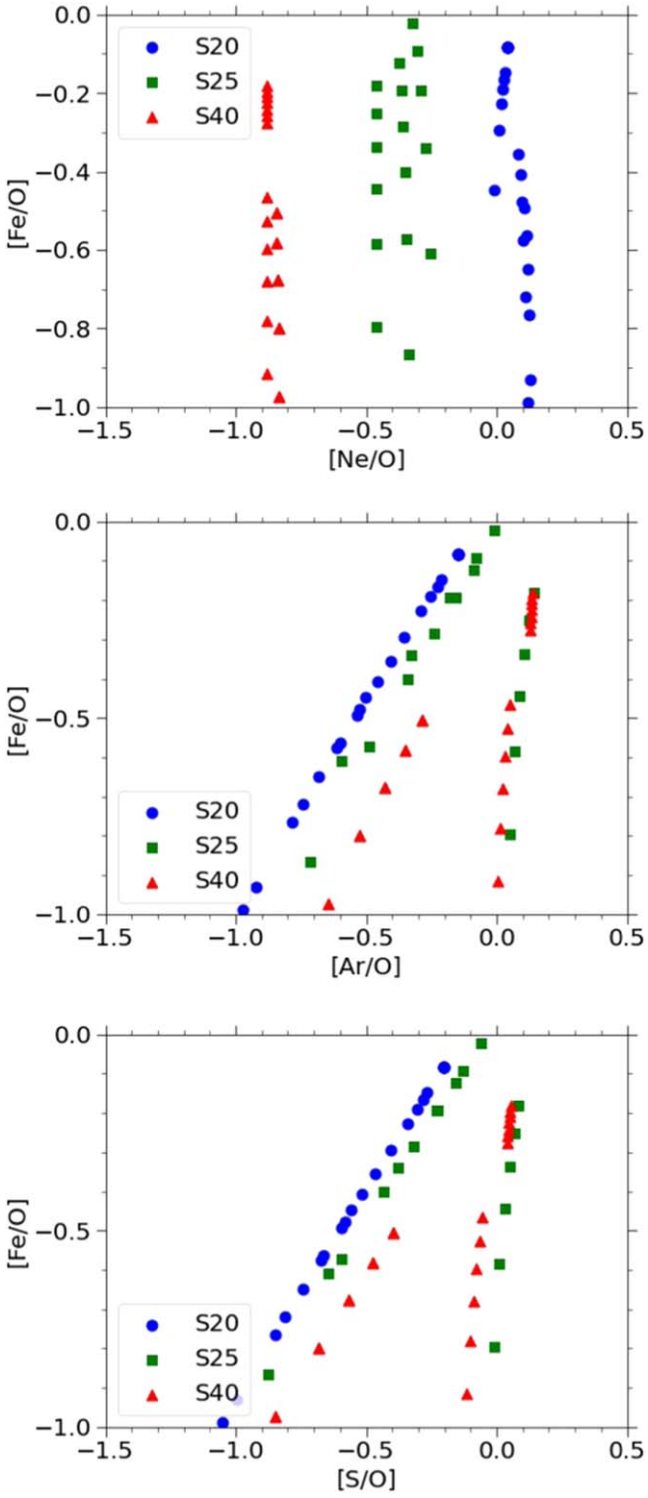

Figure 6. The nucleosynthetic yields of the 1D spherical explosion models with the mixing–fallback mechanism to approximate the aspherical yields. Mixing masses of 3–6 $M_{\odot}$ are adopted. Top panel: [Fe/O] against [Ne/O]. Middle panel: [Fe/O] against [Ar/O]. Bottom panel: [Fe/O] against [S/O].

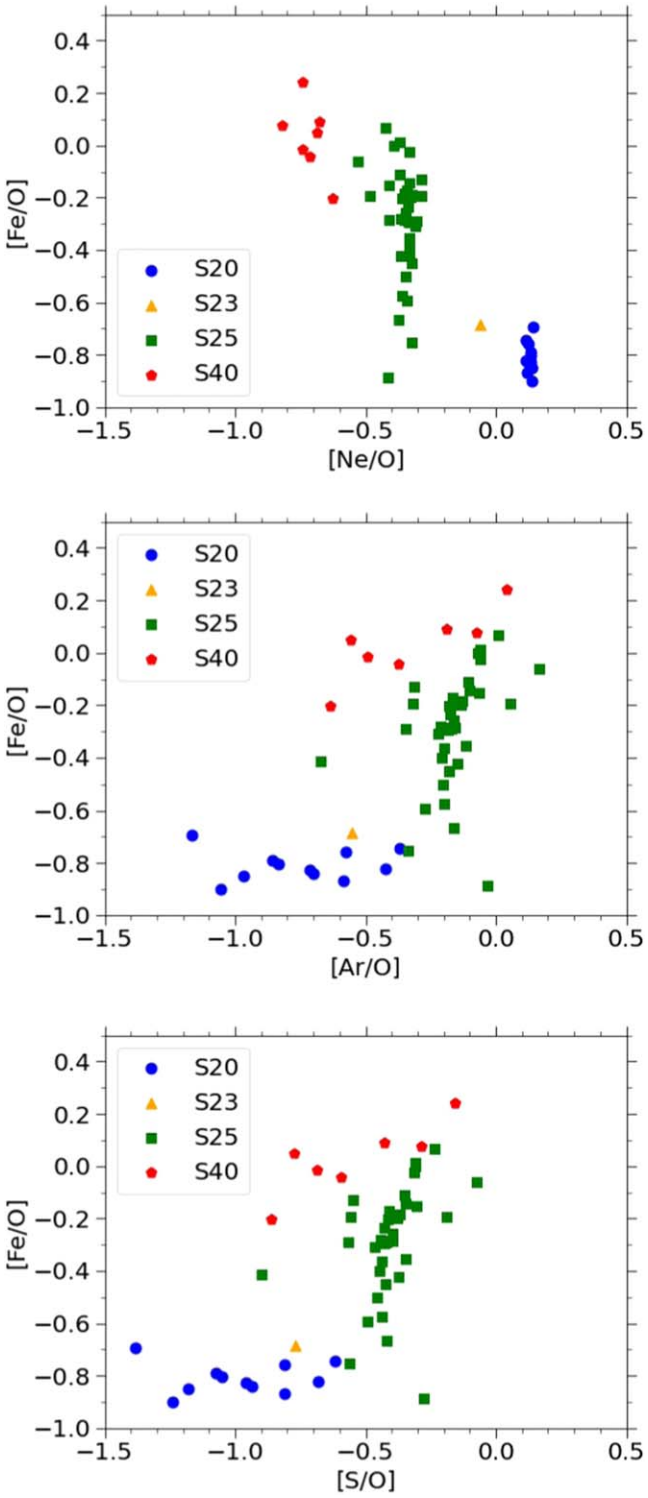

Figure 7. Same as Figure 6, but for the 2D jet-driven SN models presented in this work. Top panel: [Fe/O] against [Ne/O]. Middle panel: [Fe/O] against [Ar/O]. Bottom panel: [Fe/O] against [S/O].

(3) The 20 $M_{\odot}$ star shows distinctively lower [Fe/O], [Ar/O], and [S/O] than more massive stars because its more compact progenitor leads to very strong fallback of the Si core as we show in the next section. Such fallback suppresses the synthesis and ejection of Fe. We also observe that [Ar/O] and [S/O] are very similar to each other. The distinction of the 1D approximation and 2D models further indicates the needs of the self-consistent simulations for correctly predicting the mixing and fallback process.

3.2. Dependence on Progenitor Mass

In Figure 8 we present the distribution of the tracer particles for the 20 $M_{\odot}$ model using the standard jet energetics. The

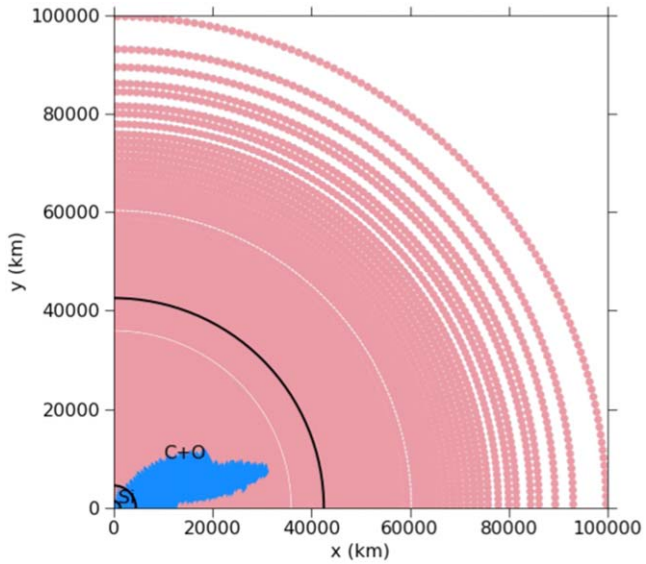

Figure 8. Same as Figure 1, but for the characteristic model of 20 $M_\odot$ as the progenitor.

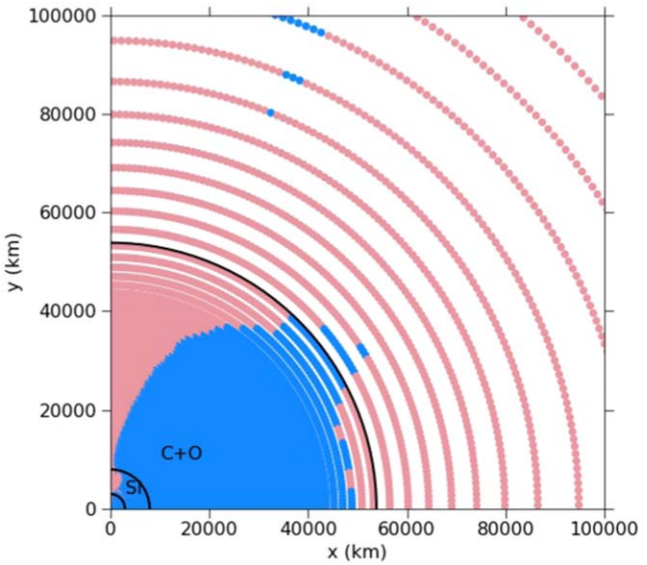

Figure 9. Similar to Figure 1, but for the characteristic model of 40 $M_\odot$ as the progenitor.

progenitor has thin Si and C+O layers at the onset of collapse. Despite this model having a lower binding energy than the 25 $M_\odot$ model counterpart, a larger fraction of the Si layer remains bound at the end of the simulation. We note that both models receive the same amount of the deposited energy. The inner C+O layer is ejected in an aspherical manner. The cone-shaped ejecta, with the energy deposition being confined within 15°, can extend beyond 45°. Matter above ∼15,000 km is fully ejected.

Similar to the above plot, we plot the tracers for the 40 $M_\odot$ model in Figure 9. The tracers that can escape show a clearer jet structure. It can be separated into two parts. Below $r \sim 30{,}000$ km, the tracers are limited to the cone similar to the jet, but with a wider open angle ∼30°. Above 30,000 km, ejecta appears to be spherical in distribution, with the exception near the boundary.

In Figure 10 we show a plot of tracers being similar to Figure 2 but including models with different progenitor masses. All three models show monotonically increasing distributions of $T_{\rm max}$ against $\rho_{\rm max}$, suggesting that the shock is propagating only outward radially, without observable reflection or collision. The 25 and 40 $M_\odot$ models are less compact than the 20 $M_\odot$ model but show similar tracer distributions. The temperature fluctuations at $\rho = 10^5$–10^7 g cm^{-3} are smaller for 25 and 40 $M_\odot$ models than for the 20 $M_\odot$ model. All models show that at $\rho > 10^6$ g cm^{-3} the tracers experience only α-rich freeze-out.

In Figure 11, we plot the mass fraction of the ejecta. The ejecta mass fraction is the mass fraction of passive tracer particles that have a positive total energy by the end of the simulation. These tracers, which are also post-processed for nucleosynthesis, are the matter to be ejected in the explosion. For each progenitor mass, the ejecta fraction tends to increase as the deposited energy increases. There are large variations among models with the same deposited energy because the robustness of the ejection depends on the shock strength, which consequently depends on the jet properties.

The ejecta mass fraction of the S20 series reaches the asymptotic value of ∼0.85 at a relatively low deposited energy of $\sim 2 \times 10^{51}$ erg. On the other hand, the more massive progenitor of the S25 series requires a higher deposited energy of $\sim 3 \times 10^{51}$ erg

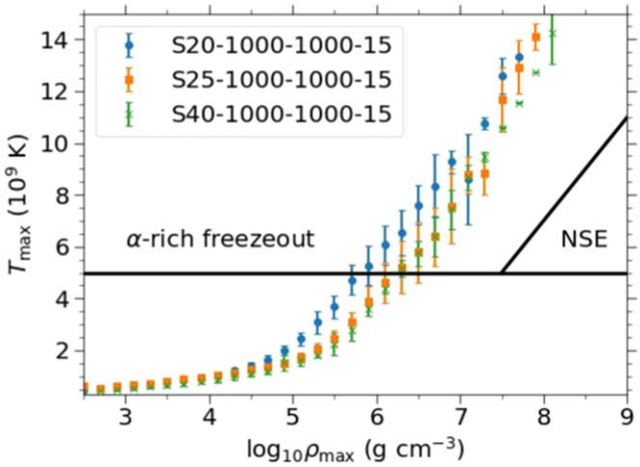

Figure 10. Same as Figure 2, but for the 20 and 40 $M_\odot$ progenitor models with the standard jet.

for the ejecta mass fraction to reach the asymptotic value of ∼0.80. The lower asymptotic value can be understood because the more massive Si core tends to be accreted regardless of the deposited energy. We remind that, due to the jet geometry, the equatorial matter in the Si core is less likely to be ejected.

In Figure 12 we plot the isotopic abundances of two contrasting models S20-1000-1000-15 (20 $M_\odot$) and S40-1000-1000-15 (40 $M_\odot$). The two models share the same jet energy but different progenitor masses. The differences of the pre-collapse structure in terms of the relative mass fractions of the C+O and Si-layers, together with their binding energies, lead to very substantial differences in the abundance patterns.

The lower-mass progenitor (20 $M_\odot$) produces such large ratios of O-group and Si-group isotopes relative to ^{56}Fe as $[(^{16}\mathrm{O},^{20}\mathrm{Ne},^{24}\mathrm{Mg})/^{56}\mathrm{Fe}] \gtrsim 1.0$ and $[(^{28}\mathrm{Si},^{32}\mathrm{S},^{36}\mathrm{Ar},^{40}\mathrm{Ca})/^{56}\mathrm{Fe}] \gtrsim 0.3$ (and thus $[(^{16}\mathrm{O}/^{24}\mathrm{Si}] \gtrsim 0.2$).

In contrast, the higher-mass progenitor (40 $M_\odot$) produces much smaller ratios of O-group and Si-group isotopes relative to ^{56}Fe, i.e., $[(^{16}\mathrm{O},^{20}\mathrm{Ne},^{24}\mathrm{Mg})/^{56}\mathrm{Fe}] \lesssim -0.1$ and $[(^{28}\mathrm{Si},^{32}\mathrm{S},^{36}\mathrm{Ar},^{40}\mathrm{Ca})/^{56}\mathrm{Fe}] \lesssim -0.4$ (and thus $[(^{16}\mathrm{O}/^{24}\mathrm{Si}] \gtrsim 0.3$).

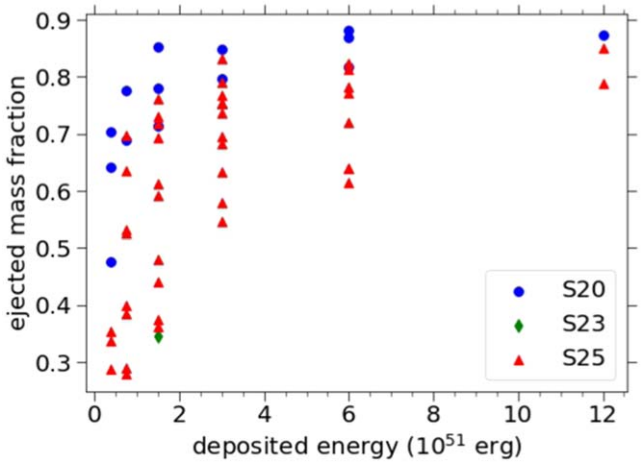

Figure 11. The ejecta mass fraction of the models in Tables 1 and 2.

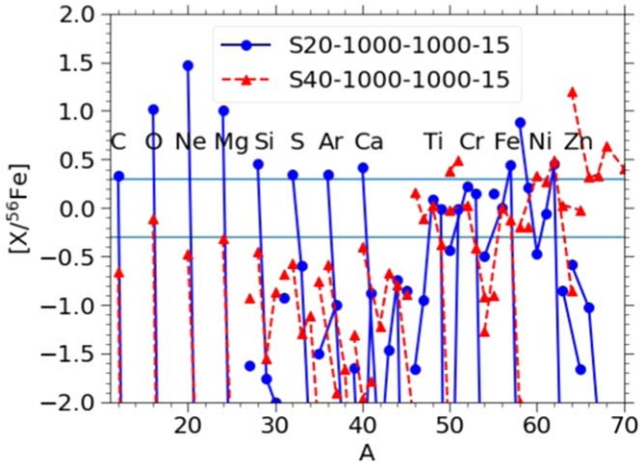

Figure 12. Chemical abundance patterns of Models S20-1000-1000-15 (20 $M_\odot$: blue solid line) and S40-1000-1000-15 (40 $M_\odot$: red dashed line).

For Fe-group isotopes, the differences are irregular. For example, the lower-mass model shows a suppressed ^{64}Zn production but an enhanced ^{58}Ni production relative to ^{56}Fe. In contrast, the higher-mass model shows opposite ratios. Such a difference is due to the difference in the Y_e distribution.

3.3. Effects of Mass Cut

In Figures 13 and 14, we plot the tracer particle distribution for the 25 $M_\odot$ star being similar to Figure 1 but with a different mass cut (i.e., inner boundary) at radii of $R_{\rm cut} = 1500$ and 2100 km, respectively. A direct comparison with Figure 1 shows a drastic difference in the ejecta mass and structure. While the two models have the same jet energy, the mass cut at the larger $R_{\rm cut}$ leads to more significant fallback, including both the Si core and the inner C+O core. The ejection of the He envelope is only mildly reduced.

The change of the mass cut to larger $R_{\rm cut}$ causes the following changes in the ejecta structure.

First, the mass cut at larger $R_{\rm cut}$ means the formation of a more massive compact object. Second, the larger $R_{\rm cut}$ leads to more mass receiving the jet energy. The final energy per unit mass after the jet deposition is lower, which means a weaker outgoing shock. The effect of $R_{\rm cut} = 2100$ km is significant.

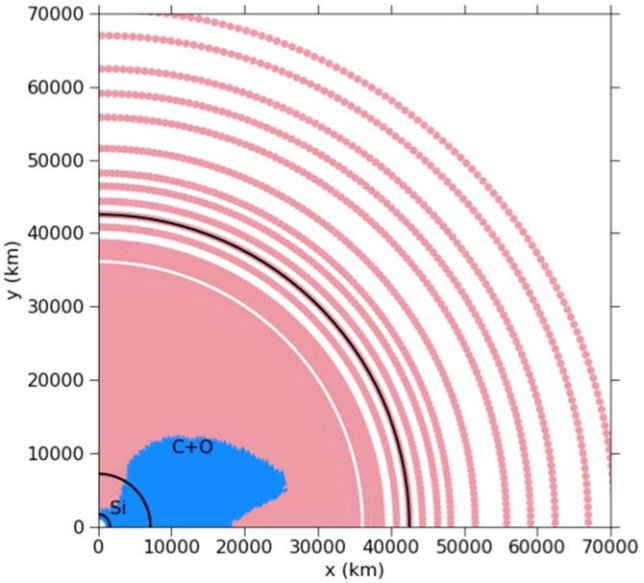

Figure 13. Similar to Figure 8, but for the mass cut at $R_{\rm cut} = 1500$ km in the 25 $M_\odot$ model with the same jet parameters.

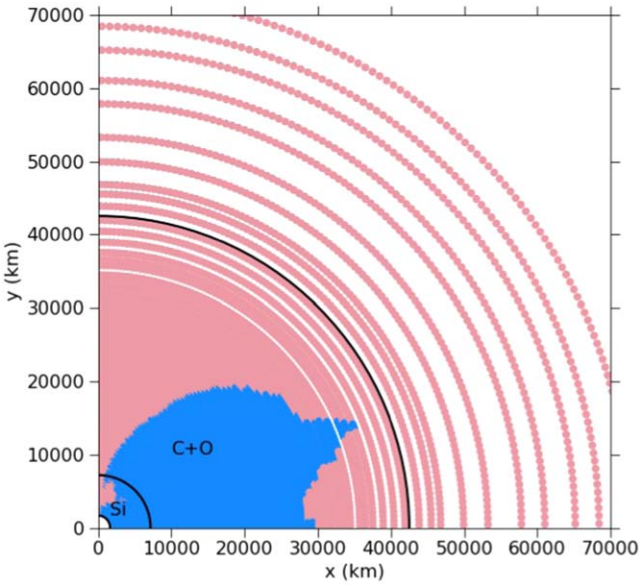

Figure 14. Similar to Figure 8, but for the mass cut at $R_{\rm cut} = 2100$ km in the 25 $M_\odot$ model with the same jet parameters.

Even with the same amount of deposited energy, the majority of the inner core fails to be ejected. Only the outskirts of the C+O core are ejected at the end of simulation.

In Figure 15 we show the thermodynamics history of our characteristic models using the 25 $M_\odot$ progenitor, but with the innermost radius of 900, 1500, and 2100 km. The maximum density experienced by the tracers is smaller for the larger inner radius. For the model with $R_{\rm cut} = 2100$ km, all tracers have densities less than 10^7 g cm^{-3}.

In Figure 16, we compare the abundance patterns with different mass cuts. It does not show qualitative differences. The two models follow each other, with the model with a more extended mass cut (1500 km) having in general 20%–50% higher O-group and Si-group elements up to Ca. The relation

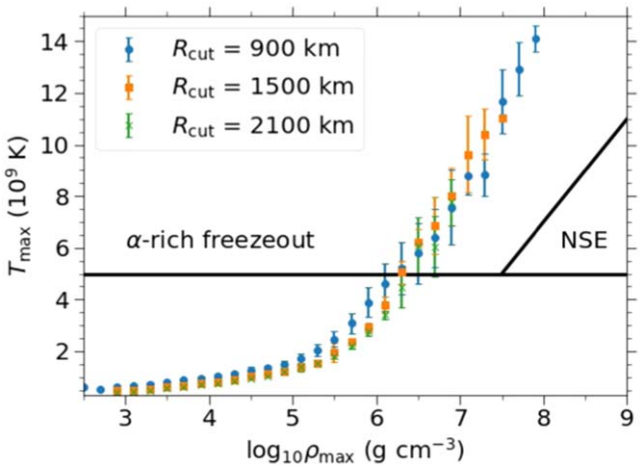

Figure 15. The tracer thermodynamics history of the characteristic model using the 25 $M_\odot$ star as the progenitor with $R_{cut} = 900$, 1500, and 2100 km at the mass cut.

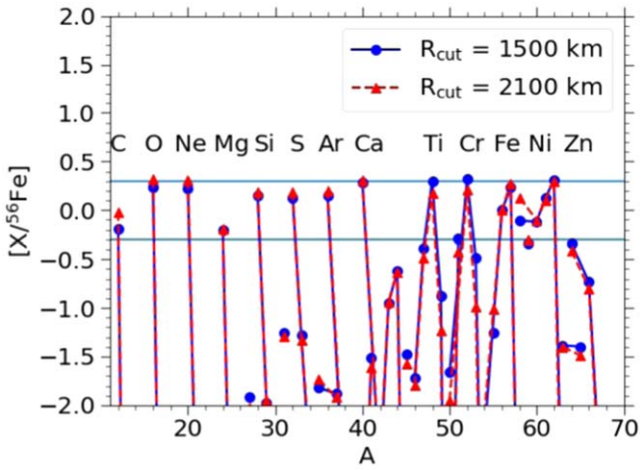

Figure 16. The chemical abundance patterns of Model S25-1000-1000 with $R_{cut} = 1500$ km (blue solid line) and $R_{cut} = 2100$ km (red dashed line).

flips for more massive elements. Two exceptions are ^{50}Cr and ^{54}Cr. The more extended mass cut can boost its production. The mild difference of the Fe-group elements, mostly from the innermost region of the star, is small in terms of the mass cut. This agrees with the ejecta distribution that the narrow segment in the Si core is ejected in both models. In addition, the accreted matter is mostly C+O-rich matter, which does not bring major nucleosynthetic changes to other elemental abundances.

4. Discussion

4.1. The Ti–V Relation Revisited

C. Sneden et al. (2016) have found that [Ti/Fe] and [V/Fe] show a correlation of 45° based on the metal-poor star catalog derived in I. U. Roederer et al. (2014) (Figure 17). In S.-C. Leung et al. (2023), we have explored the [Ti/Fe]–[V/Fe] relation using the 40 $M_\odot$ models and compared with the observed relation. In our previous work, the 45° relation is reproduced, but the interception differs from the data.

In Figure 17, we extend our comparison with the available data by including our new models. Being consistent with our

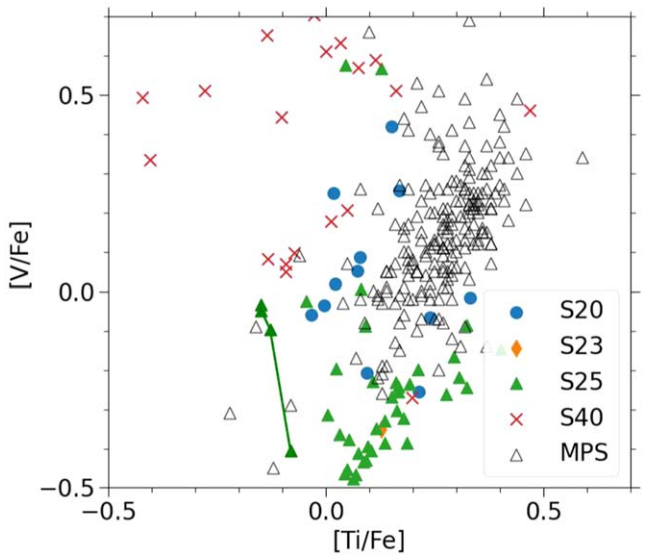

Figure 17. The [V/Fe] against [Ti/Fe] relation for the jet-driven SN models in this work. The semitransparent purple diamonds stand for the metal-poor star data taken from I. U. Roederer et al. (2014). The straight line connects the spherical explosion models of S25 with different explosion energies.

40 $M_\odot$ models, there is also a clear trend in our 25 $M_\odot$ models, which also show a 45° inclination in the [Ti/Fe]–[V/Fe] plane. The 20 $M_\odot$ series of models, on the contrary, does not show a clear trend, but their composition is closer to the cluster formed by the observational data. The 40 $M_\odot$ models are in general very remote to those EMP stars. They have a much higher [V/Fe] ratio.

To compare with the spherical explosion models, we also show one particular mass of 25 $M_\odot$ with different explosion energy. It shows that in the high-energy limit the spherical model resembles our aspherical models. This agrees with our expectation that the jet model can create high-entropy matter that is similar to a very strong explosion in the spherical case.

If we extend the data assuming a linear trend, the intercepts of models with different progenitor masses do not vary monotonically. This is because in the lower-mass models the Fe production is affected by the more prominent fallback. This suggests a nonlinear competition between lowering the mass and the enhanced production of [Ti/Fe]. A further inspection will be useful for exploring the mass dependence of this element pair.

4.2. ^{56}Ni Mass and Ejecta Mass Relation

An interesting relation for Type Ib/c SNe is the correlation between the ejected ^{56}Ni mass (M_{56}) and the ejecta mass (M_{ej}). These two quantities can be well extracted from the light curve. Qualitatively, the peak brightness and the width of the light curve determine the M_{56} and M_{ej}, respectively. In the Intermediate Palomar Transient Factory (iPTF) surveys presented in A. De Cia et al. (2018), F. Taddia et al. (2019), and S. Gomez et al. (2022), a clustering is observed for this kind of SN. Here we examine whether a similar relation can be reproduced for the jet-driven models.

In Figure 18, we plot the M_{56}–M_{ej} relation for the catalog in this work and the surveys described above. It shows that models with different progenitor masses have significant overlap in the parameter space as follows: (1) The S20 series does not exhibit large variations, and it is suitable to explain the

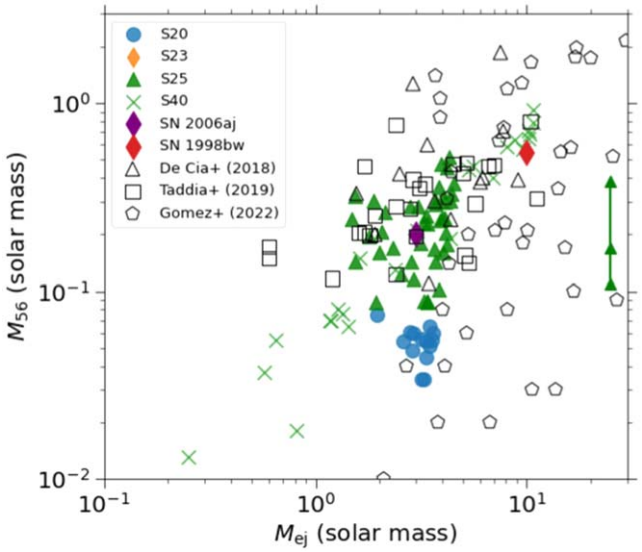

Figure 18. The ejected ^{56}Ni mass (M_{56}) against the ejecta mass (M_{ej}) of the jet-driven SN models in this work (20 $M_\odot$ series: blue circles; 23 $M_\odot$ series: orange diamonds; 25 $M_\odot$ series: green triangles; 40 $M_\odot$ series: green crosses). The plot is overlaid with the observed Type Ib/c SN catalog taken from A. De Cia et al. (2018; brown triangles), F. Taddia et al. (2019; pink squares), and S. Gomez et al. (2022; gray pentagons). The green triangles connected with the line are the spherical explosions of the S25 models with different explosion energies.

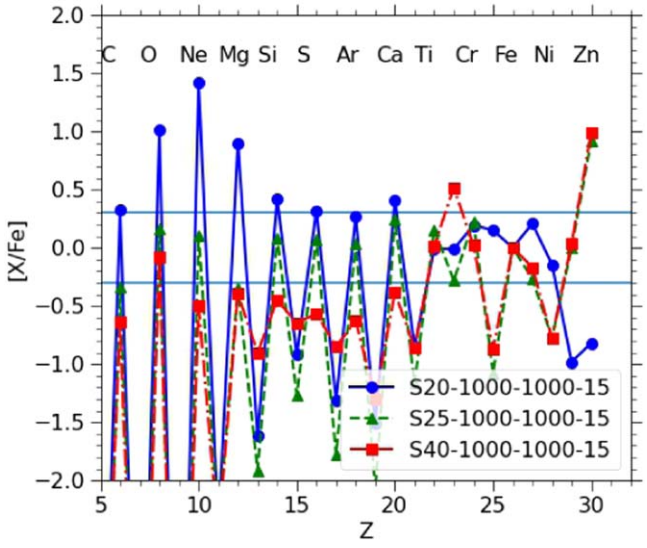

Figure 19. The elemental abundances [X/Fe] of our characteristic models using 20 $M_\odot$ (blue solid line, circle), 25 $M_\odot$ (green dashed line, triangle), and 40 $M_\odot$ (red dotted–dashed line, square) models. The two lines correspond to 50% and 200% of the solar value.

faint SNe of $M_{56} < 0.1\,M_\odot$ with $M_{ej} = 0.1$–$0.5\ M_\odot$. (2) The S40 series has a clear rising trend of M_{56}. (3) The S25 series has M_{56} less sensitive to M_{ej}. The contrast among these series is related to the compactness of the progenitor model. In a lower-mass model, the higher compactness leads to strong fallback in the inner core.

By observing how the theoretical data overlap with the observational data, we conclude that the 25 $M_\odot$ series agrees with the observed Type Ib/c SNe from F. Taddia et al. (2019) and S. Gomez et al. (2022). These SNe (including the well-observed SN 1998bw and SN 2006aj) have typically $M_{56} \sim 0.1$–$1\ M_\odot$ and $M_{ej} = 1$–$10\,M_\odot$. However, the jet-driven SN cannot explain directly the data point with an $M_{ej} > 0.5\,M_\odot$ and a low M_{56} ($<0.1\,M_\odot$). Similarly, this model cannot fully explain SNe with high M_{56} ($>1\,M_\odot$).

We also include the spherical explosion model for the S25 progenitor shown by the triangles with a line. The high explosion energy makes the entire envelope ejected. Thus, M_{ej} does not change significantly across different explosion energies. M_{56} increases sharply as the explosion energy increases. The high M_{ej} does not well resemble the clustering of the data.

4.3. Elemental Abundance of Jet-driven Supernovae

In the previous sections, we have presented the detailed isotopic abundances of our models. In this section, we compare our results with some well-observed metal-poor galaxies. These galaxies, some of which have relatively low metallicity, are good test cases for our zero-metallicity models because such early galaxies might have a much lower fraction of metal enrichment by Type Ia SNe. Most explosions are contributed by either spherical and aspherical massive-star explosions. Therefore, this reduces the dependence on some of the uncertain parameters in Type Ia SNe, such as the explosion channel (S.-C. Leung & K. Nomoto 2023) and the delay time (C. Kobayashi et al. 2020).

In Figure 19 we aggregate the abundances element-wise and plot the elemental abundance patterns. The graph provides a direct comparison with observational data because the spectral lines from galaxies do not distinguish the detailed distribution across stable isotopes. Nonetheless, we stress that the isotopic distribution is equally important because it allows us to clarify the explosion physics quantitatively.

Figure 19 shows that [(C–Ca)/Fe] > 0.3 in the 20 $M_\odot$ model while [(C–Ca)/Fe] < -0.1 in the 40 $M_\odot$ model. The 25 $M_\odot$ model has the chemical abundance most proximate to the solar abundance pattern. All three models show a comparable Fe-group element production, with the exception near Zn. The higher-mass model tends to produce more Zn than the lower-mass models.

5. Comparison with Observational Data

5.1. Extremely Metal-poor Galaxies

In K. Watanabe et al. (2024) EMPRESS continues to analyze the chemical abundances of some metal-poor galaxies. The analysis includes two new objects, SBS-0335-052E and J0125 +0759. In Table 5 we list the abundance data of these galaxies, together with some other metal-poor galaxies collected from relevant surveys. Similar to J. Mao et al. (2021), Ne, Ar, S, and Fe relative to O are measured. We list the galaxies we have used for our comparison in Table 5.

Table 6 lists the EMP galaxy studied in this work. We focus on the samples that have good measurements of the Ne/O and Ar/O ratios. Among these EMP galaxies, they share similar values of $\log_{10}$ Ar/O ~ -2.3, which is significantly subsolar. Their Ne/O ratio $\log_{10}$ Ne/O ~ -0.6 is slightly subsolar. The relatively flat distribution of the Ar/O ratio among these galaxies suggests that these galaxies have experienced similar metal enrichment history.

We should note that, for abundance comparisons between EMP galaxies and theoretical models, we need chemical evolution models of galaxies as mentioned in K. Watanabe et al. (2024).

Table 5
The Chemical Abundance Data of Some Extremely Metal-poor Galaxies Collected from Recent Works as Reported in K. Watanabe et al. (2024)

Galaxy ID	[Ne/O]	[S/O]	[Ar/O]	[Fe/O]	References
SBS-0335-052E	-0.27 ± 0.00	$0.018^{+0.05}_{-0.018}$	$-0.037^{+0.02}_{-0.03}$	$-0.24^{+0.11}_{-0.24}$	K. Watanabe et al. (2024)
J0125+0759	-0.01 ± 0.00	-0.34 ± 0.05	$-0.08^{+0.01}_{-0.08}$	$-0.24^{+0.12}_{-0.24}$	K. Watanabe et al. (2024)
J0159-0622	$-0.12^{+0.01}_{-0.02}$	-0.016 ± 0.06	-0.01 ± 0.02	$-0.51^{+0.17}_{-0.28}$	Y. Isobe et al. (2022)
J1608+4337	0.107 ± 0.02	-0.07 ± 0.02	$-0.04^{+0.02}_{-0.03}$	$-0.43^{+0.15}_{-0.22}$	Y. Isobe et al. (2022)
J2115–1734	$0.003^{+0.004}_{-0.005}$	-0.079 ± 0.06	$0.04^{+0.01}_{-0.06}$	$-0.41^{+0.03}_{-0.02}$	T. Kojima et al. (2020)
J0811+4730	-0.0048 ± 0.031	-0.117 ± 0.056	-0.245 ± 0.104	0.17 ± 0.092	Y. I. Izotov et al. (2018)

Table 6
Elemental Abundance Data of EMP Galaxies Used in This Work, as Extracted in Y. Isobe et al. (2022)

EMP Galaxy	$\log_{10}$(Ne/O)	$\log_{10}$(Ar/O)	$\log_{10}$(Fe/O)
J0156–0421	−0.759	−2.39	< -0.45
J0159–0622	−0.878	−2.32	−1.74
J0210–0124	−0.688	−2.37	−1.75
J0226–0517	−0.664	−2.38	−1.27
J0232–0248	−0.692	−2.42	−1.26

In the present work, we make a simple comparison between the ∼20–40 $M_\odot$ Population III stars and EMP galaxies in order to study how important the jetlike explosions are for chemically enriching EMP galaxies. In addition, ∼20–25 $M_\odot$ stars have been shown to make the largest contribution in chemical evolution of galaxies (T. A. Weaver et al. 1978; S. E. Woosley & T. A. Weaver 1995).

In Figure 20 we compare the post-explosion nucleosynthesis of our spherical models from 20 to 40 $M_\odot$ for different explosion energies. We demonstrate the mismatch between the "spherical" explosion models and EMP galaxies. We note that the lower-mass star tends to produce larger [Ne/O] with a weak dependence on the explosion energy, and the higher-energy explosion produces smaller [Ar/O].

The progenitor mass dependence of [Ne/O] stems from the C/O ratio after He burning, which is smaller for a higher mass because of the higher temperature during He burning. The trend of [Ar/O] is expected because a higher explosion energy implies a stronger shock and a higher post-shock temperature, which burn more O into Si, S, and Ar. This facilitates the fusion of the C+O core into elements beyond Ar. Among all models, only the models ∼20–30 $M_\odot$ have [Ne/O] close enough to the observational data. However, their [Ar/O] is too high, with the exception of one 30 $M_\odot$ model of low explosion energy.

In Figure 21, [Ar/O] against [Ne/O] is plotted for the jet-driven models presented in this work and the EMP galaxy data. The horizontal spread of the observed data shows that [Ar/O] is insensitive to [Ne/O] and is higher than in the theoretical models. This implies that there is some input physics in the stellar evolutionary models that leads to a systematically smaller [Ar/O]. [Ne/O] has a very small uncertainty. Based on their values, we can infer that the peak progenitor mass that contributes to the observed abundance is between 20 and 25 $M_\odot$. [Ne/O] of these EMP galaxies suggest that they have the SN contribution centered around 23 $M_\odot$ stars in their chemical evolution.

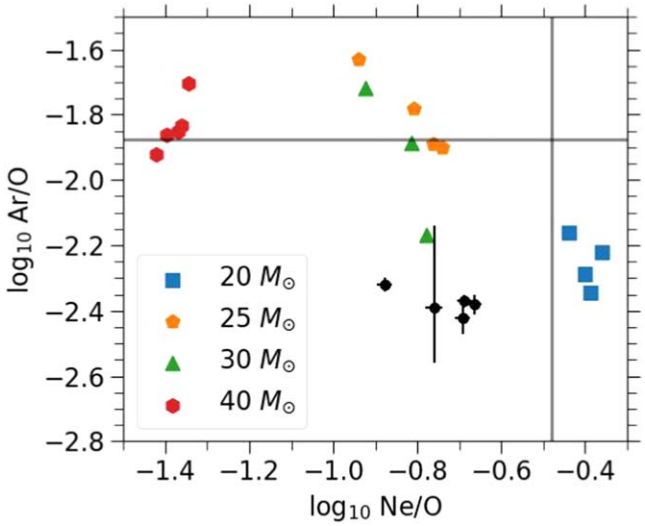

Figure 20. The comparison of the post-explosion [Ne/O] against [Ar/O] for selected EMP galaxies and the "spherical" explosion models. The straight line stands for the solar values of the corresponding isotope ratios. The data points correspond to the EMP galaxies reported in Y. Isobe et al. (2022).

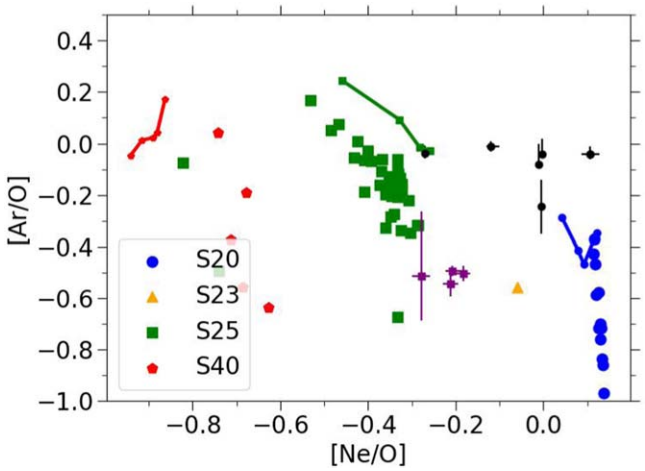

Figure 21. [Ar/O] against [Ne/O] for the jet-driven SN models in this work, compared with the EMP galaxy catalog presented in K. Watanabe et al. (2024; black circles with error bars) and in Y. Isobe et al. (2022; purple squares with error bars). The colored lines stand for the sequence of 1D models with different explosion energies.

We also compare our models with the data points from Y. Isobe et al. (2022; purple squares with error bars). This element pair also demonstrates a clear clustering for this data set. The clustering of the data point suggests that these galaxies have a large contribution of the 25 $M_\odot$ star explosion in their

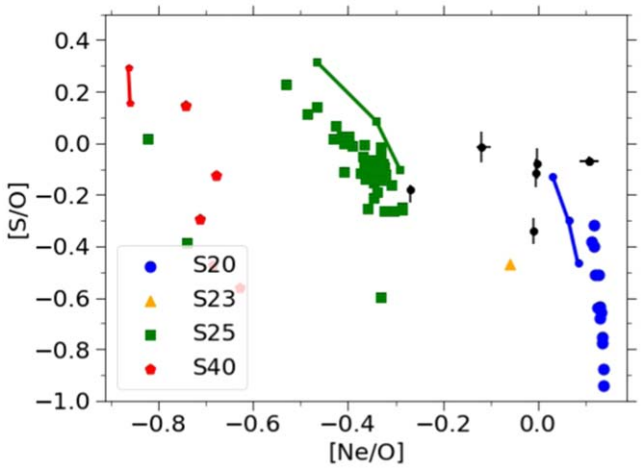

Figure 22. Same as Figure 21, but for [S/O] against [Ne/O].

chemical evolution. The comparison can be similarly made for the data points from K. Watanabe et al. (2024; black circles with error bars). These data points have [Ne/O]~ -0.1–0.1, which lie somewhere between the clusters of 20 and 25 $M_{\odot}$ star explosions. Their high [Ar/O] suggests that these EMP galaxies require contributions from the high-energy explosions of these two groups.

In Figure 22, we plot [S/O] against [Ne/O] for the same sequences of input models. The observational data show that both ratios have a narrow range of -0.4 to 0.0, being similar to the solar abundance. The range of [S/O] is consistent with the jet-driven models. The spread of the S25 models is similar to that for the observed galaxies.

In the top panel of Figure 23, we plot [Fe/O] against [Ne/O] for the same sequences of input models. The observed [Fe/O] shows larger uncertainties compared to the [Ar/O] and [S/O] data. It is interesting to note, that despite the extremely low metallicity in these galaxies, their [Fe/O] does not significantly differ from the solar value. The jet-driven models again produce a spread consistent with the observed range of the abundance ratios.

In the middle panel of Figure 23, we compare [Fe/O] against [Ar/O], alongside the observational data. Different from [Ne/O], the numerical data cluster at [Ar/O] $= -1.0$ to 0. A lower-mass model tends to have a lower [Ar/O]. The numerical models coincide well with galaxy abundances from K. Watanabe et al. (2024). There are three galaxies reported in Y. Isobe et al. (2022), and all of them show [Ar/O] around -0.5. The data with low [Fe/O] overlap with the 20 $M_{\odot}$ spherical explosion models.

The figure can be further compared with the first panel of Figure 2 of K. Watanabe et al. (2024). In their work, they compare various massive-star explosion models with the galaxies they observed. They show that the spherical models require parameterized "mixing and fallback" in order to reproduce the observed abundance ratio, or require contributions of Type Ia SNe to match the observed [Fe/O]. Our models show that with the jet-driven explosion the theoretical models may reach the observed high value of [Fe/O].

In the bottom panel of Figure 23, we plot [Fe/O] against [S/O] as in the second panel of Figure 2 of K. Watanabe et al. (2024). The numerical models show a scatter of [S/O] being similar to [Ar/O], because both elements are Si-group elements. We notice that a lower-mass model generates a smaller [S/O]. The 1D models tend to synthesize too much

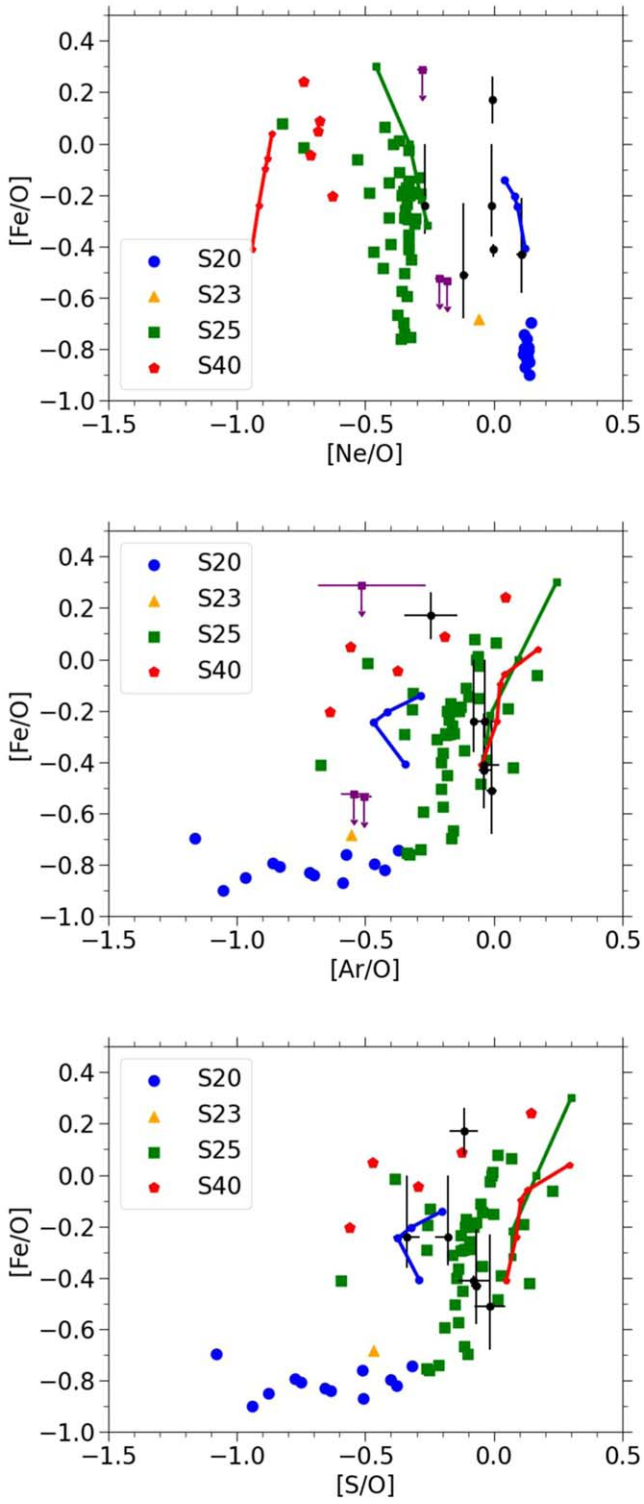

Figure 23. Top panel: same as Figure 21, but for [Fe/O] against [Ne/O]. Middle panel: same as the top panel, but for [Fe/O] against [Ar/O]. Bottom panel: same as the top panel, but for [Fe/O] against [S/O].

[S/O] but not enough [Fe/O] in this parameter space. In contrast, some galaxy samples match very well with the jet-driven explosion models.

By cross-examining these three figures, it suggests that the aspherical explosion could provide a clue to understanding the unique chemical abundance patterns of these metal-poor galaxies.

Table 7
Selected Extreme Metal-poor Stars from M. Jeong et al. (2023)

EMP ID	[Fe/H]	[Mg/Fe]	[Ca/Fe]	[Cr/Fe]	[Ni/Fe]	Classification
J0010	-2.48 ± 0.11	0.73 ± 0.04	0.19 ± 0.05	-0.10 ± 0.05	0.13 ± 0.05	VMP
J0158	-3.04 ± 0.05	0.06 ± 0.06	0.41 ± 0.04	-0.09 ± 0.06	0.30 ± 0.06	EMP
J0357	-2.75 ± 0.05	0.34 ± 0.04	0.33 ± 0.03	-0.16 ± 0.05	0.37 ± 0.07	EMP
J0713	-3.15 ± 0.08	0.31 ± 0.06	0.00 ± 0.05	-0.33 ± 0.03	-0.01 ± 0.04	EMP
J0814	-3.39 ± 0.05	0.33 ± 0.04	0.61 ± 0.07	-0.33 ± 0.03	-0.01 ± 0.04	EMP
J0908	-3.67 ± 0.06	0.17 ± 0.07	0.35 ± 0.04	-0.47 ± 0.08	0.35 ± 0.08	EMP
J1037	-2.50 ± 0.05	0.30 ± 0.03	0.12 ± 0.03	-0.24 ± 0.09	0.34 ± 0.09	CEMP
J1317	-2.37 ± 0.05	0.30 ± 0.06	0.24 ± 0.05	-0.09 ± 0.11	0.69 ± 0.06	VMP
J1650	-2.17 ± 0.05	0.13 ± 0.07	0.35 ± 0.04	-0.22 ± 0.10	0.73 ± 0.10	VMP
J2242	-3.40 ± 0.08	0.24 ± 0.04	0.71 ± 0.14	0.01 ± 0.26	0.89 ± 0.36	EMP

Note. The classifications include VMP (very metal-poor stars: [Fe/H] < -2), EMP (extremely metal-poor stars: [Fe/H] < -3), and CEMP (carbon-enhanced metal-poor stars: [C/Fe]>1.0).

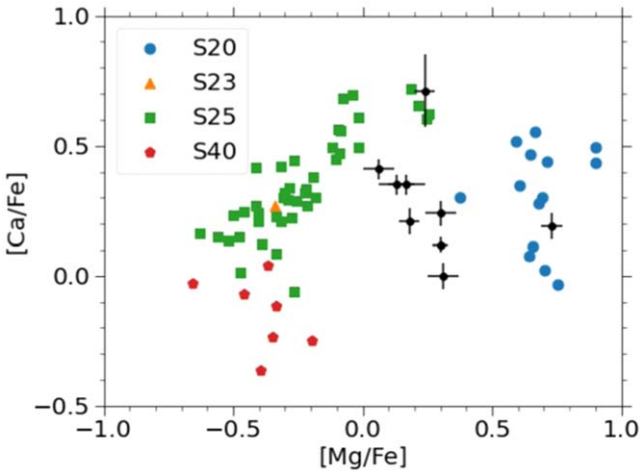

Figure 24. [Ca/Fe] against [Mg/Fe] for the EMP star analyzed in M. Jeong et al. (2023; black circle with error bars). Other data points are the theoretical models reported in this work and S.-C. Leung et al. (2023).

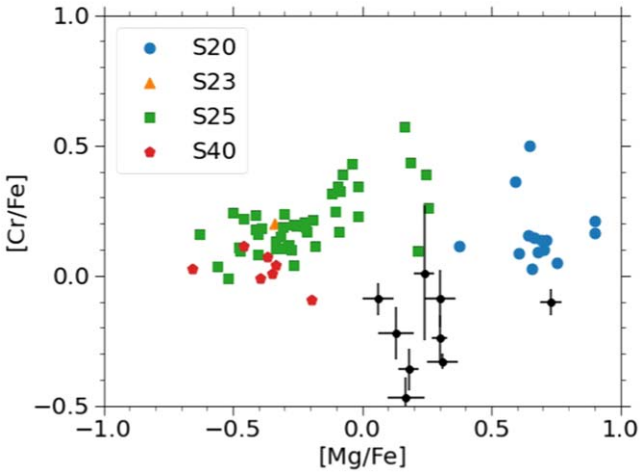

Figure 25. Same as Figure 24, but for [Cr/Fe] against [Mg/Fe].

5.2. Extremely Metal-poor Stars

Another ideal test case for massive-star nucleosynthesis is EMP stars. Similar to EMP galaxies, the elemental abundances of these old stars correspond to one or a few massive-star explosions. The contribution of Type Ia SNe remains less important. However, due to their small length scale, the inhomogeneous mixing and the angle dependence of the aspherical explosion could be important.

Recently, M. Jeong et al. (2023) analyzed the high-resolution spectra from stars by the legacy Sloan Digital Sky Survey (SDSS; D. G. York et al. 2000) and the Large sky Area Multi-Object Fiber Spectroscopic Telescope (LAMOST; X.-Q. Cui et al. 2012). They identified 18 very metal-poor (VMP) stars, 10 EMP stars, and 3 CEMP stars, and they performed follow-up observations with the Gemini Remote Access to the CFHT ESPaDOnS Spectrograph (GRACES; A.-N. Chené et al. 2021). We selected the stars with complete measurement of Mg, Ca, Cr, and Ni in Table 7 with a list of stars taken from their catalog.

In Figure 24, we plot [Ca/Fe] against [Mg/Fe]. Mg is synthesized by C burning, and its mass depends on the C/O ratio, which depends on the progenitor mass as is the case for Ne. Thus, this ratio is good for distinguishing the lower-mass stars (20 $M_\odot$) and the higher-mass stars (25 and 40 $M_\odot$). Different jet deposition schemes provide such a narrow range of [Ca/Fe] variation as $\sim 0-0.5$. The observed stellar data are populated between the lower- and higher-mass groups of stars. This suggests that the abundances in these observed stars were influenced by the products of stars in the mass range of $20-25\,M_\odot$ (or the mixture of the two classes of explosion). However, one particular EMP star, J2242, has an exceptionally high [Ca/Fe]. None of our models can reproduce such a high value. On the other hand, the EMP star J0010 is likely to be solely influenced by a 20 $M_\odot$ star explosion.

Figure 25 is similar to Figure 24, but for [Cr/Fe] against [Mg/Fe]. Our models show little variation of [Cr/Fe] across different progenitor and explosion models. Most metal-poor stars selected have [Cr/Fe] similar to the theoretical models, except some have a lower value by 0.25 dex.

Figure 26 is similar to Figure 24, but for [Ni/Fe] against [Mg/Fe]. There is a clear distinction between the two classes of models. The lower-mass models produce [Ni/Fe] $\gtrsim 0.3$, while the higher-mass models produce [Ni/Fe] $\lesssim 0.3$. This is related to the initial compactness of the pre-explosion progenitor. A lower-mass star has a higher central density, thus undergoing more electron capture. Therefore, the explosion produces more neutron-rich species, i.e., ^{58}Ni. Some EMP stars again are located between the two groups, further suggesting the mixed

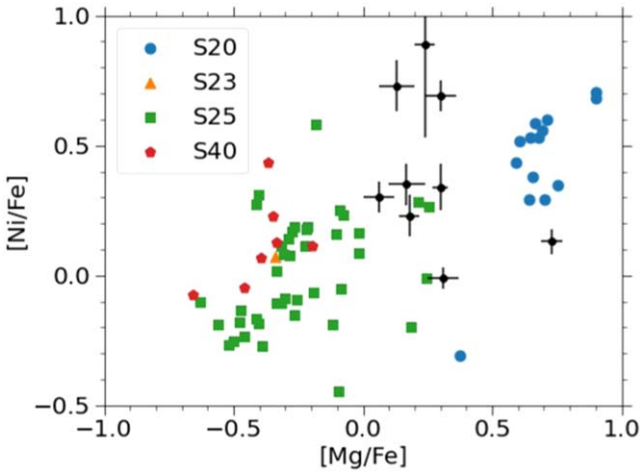

Figure 26. Same as Figure 24, but for [Ni/Fe] against [Mg/Fe].

background of massive stars. Some EMP stars exhibit very high [Ni/Fe], e.g., J1317, J1650, and J2242. Since Ni and Fe are synthesized similarly in the inner part of the ejecta, while Cr is produced near the center of the ejecta , the high [Ni/Fe] could imply different explosion mechanisms.

5.3. Metal-poor Star J1010+2358

The Galactic halo star J1010+2358 was discovered by the LAMOST survey (G. Zhao et al. 2006, 2012) and confirmed to be a VMP star with [Fe/H] = −2.42 (Q.-F. Xing et al. 2023). It has an unusually low [Mg/Fe] ∼ −0.66, which makes it distinctive from typical Galactic halo stars. In the discovery paper, element ratios against Fe, including Mg, Si, Ca, Ti, Cr, Mn, Fe, Co, and Ni, are reported. The low [Mg/Fe] and [Mn/Mg] suggest fewer contributions from Type Ia SNe and canonical CCSNe. A high-mass CCSN produces too high [Mn/Fe] and [Co/Fe], which are less compatible with the observed abundances. They further show that the yield patterns are compatible with the 260 $M_{\odot}$ PISNe in A. Heger & S. E. Woosley (2002). A recent analysis from P. N. Thibodeaux et al. (2024) favors an origin from low-mass CCSNe. The late-time high-resolution Very Large Telescope/UVES spectra where 3D effects and non-LTE effects are accounted for also suggest high C and Al abundances that rule out the pair-instability origin (Skúladóttir et al. 2024).

In Q.-F. Xing et al. (2023), the spherical explosion models are compared with this VMP star. As our models suggest that the aspherical explosion in jet-driven supernovae can lead to distinctive chemical abundance patterns, we extend the search to our jet-driven SN models. We use the measured elements as the constraints, and we look for the best-fit models by using the χ^2 fitting.

In Table 8 we show our χ^2 fitting results for LAMOST J1010+2358 using the abundances derived in the three works. The data from Q.-F. Xing et al. (2023) have the closest abundance pattern to our model with the lowest χ^2 score. Model S25-2000-1000-30 is the best-fit model. The new data derived in P. N. Thibodeaux et al. (2024) and Skúladóttir et al. (2024) show a slightly larger discrepancy for the best-fit models. Both sets of data suggest 40 $M_{\odot}$ models. The unique features in J1010+2358 strongly exclude the interpretation with the lower-mass CCSN (20 $M_{\odot}$) or direct 1D spherical explosions. We also show in Table 9 our comparison results. It

Table 8
The χ^2 Fitting Results and the Best-fit Models for LAMOST J1010+2358 from Various Derived Abundances in the Literature

Series	Source	Best-fit Model	χ^2	Best
20	a	S20-0250-1000-15	64.38	
25	a	S25-2000-1000-30	25.15	✓
40	a	S40-1000-2000-15	27.18	
Spherical	a	25 ($E_{\rm exp,51}$ = 5)	32.39	
20	b	S20-0250-1000-15	130.20	
25	b	S25-2000-0500-30	57.64	
40	b	S40-1000-0500-15	33.12	✓
Spherical	b	25 ($E_{\rm exp,51}$ = 10)	58.40	
20	c	S20-0250-1000-15	118.84	
25	c	S25b-1000-1000-30	69.58	
40	c	S40-1000-1000-15	46.76	✓
Spherical	c	30 ($E_{\rm exp,51}$ = 20)	90.78	

Note. "Source" corresponds to the literature work we used for comparing with this VMP star, with "a," "b," and "c" standing for Q.-F. Xing et al. (2023), P. N. Thibodeaux et al. (2024), and Skúladóttir et al. (2024), respectively.

Table 9
The Best-fit Models from Our Numerical Models Based on Each Massive-star Progenitor Based on χ^2 Fitting Using the 11 Element Ratios as Constraints

Explosion	$M_{\rm ZAMS}$	Model	χ^2
Jet	20	S20-0250-1000-15	64.38
Jet	25	S25-2000-1000-30	25.15
Jet	40	S40-1000-2000-15	27.18
Spherical	25	$E_{\rm exp}$ = 5 × 10^{51} erg	32.38

Note. The column "Explosion" stands for whether the 2D jet or the 1D spherical explosion is used. The "Model" column gives the best-fit model for that progenitor.

shows that the parameters close to the characteristic model can already provide a close fit to this object. The best-fit model is found to be $M_{\rm ZAMS} = 25\,M_{\odot}$.

In Figure 27 we show our comparisons. In the top panel, we plot the data points from LAMOST J1010+2358 interpreted in Q.-F. Xing et al. (2023), together with the best models from our 25 and 40 $M_{\odot}$ and spherical model series. The models represent those of the minimum χ^2. For the 1D model, it can fit the Mg and Ca. But its predictions of Ti, Cr, Ni, and Zn are too high to be compatible. The 25 $M_{\odot}$ model is the best model among all interpretations and mass sequences. The pattern essentially mimics all elements, with an exception for Ti and Cr. The 40 $M_{\odot}$ model has a similar pattern but has too high [Ti/Fe], [Cr/Fe], and [Zn/Fe] to match the VMP star. We remarked that Zn/Fe in the model is sensitive to the mass cut, so that the comparison of Zn/Fe cannot rule out the model of Zn/Fe.

In the middle panel, we plot data points similar to those in the top panel but for the data set derived in P. N. Thibodeaux et al. (2024). Their data set does not contain Si and contains a lower Ca and higher Ti, Mn, and Co. The data set also contains values for Sc. The 25 $M_{\odot}$ model cannot match the high [Sc/Fe] and [Mn/Fe] observed in that star. The 40 $M_{\odot}$ model, being the best-fit model, can track all the elements, except that the [Mn/Fe] in our model is too low to match the close-to-solar value in the VMP star. In general, our model predicts a subsolar value of [Mn/Fe] because Mn is in general a decay product of ^{55}Co,

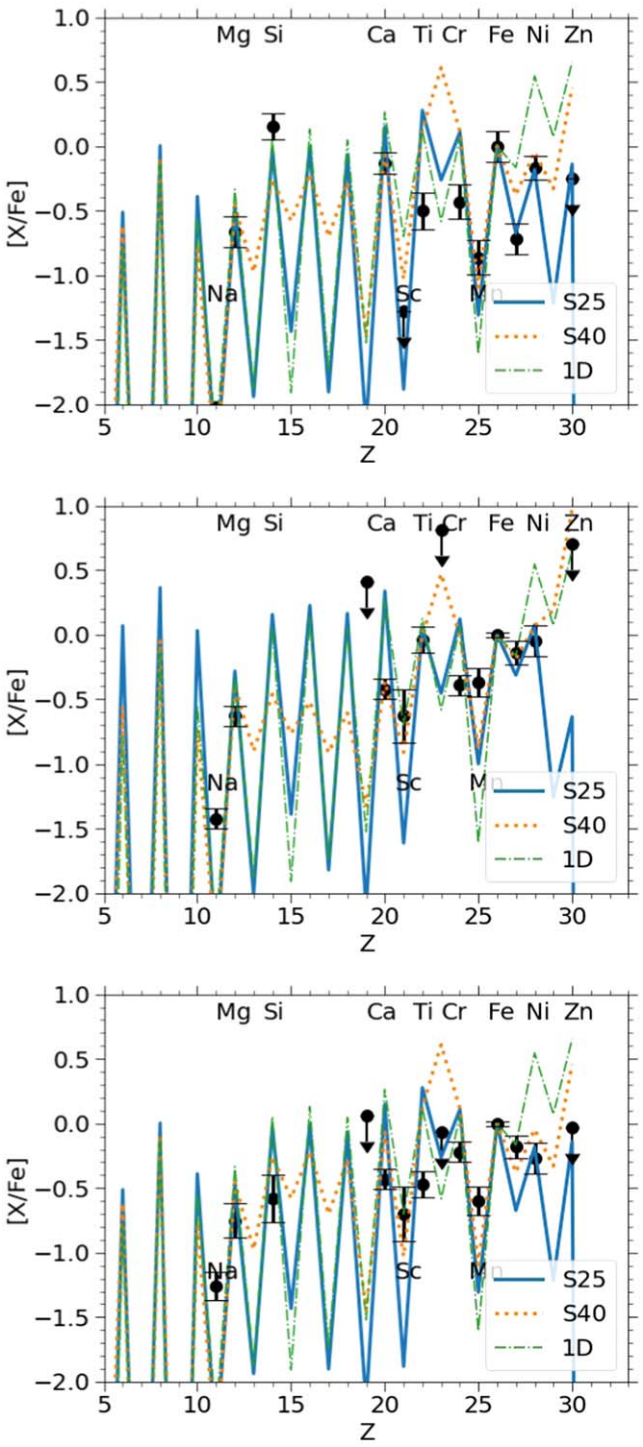

Figure 27. Top panel: the chemical abundance of J1010+2358 (circles with error bars; Q.-F. Xing et al. 2023) and the best-fit models searched from the jet-driven SN models with $M_{\rm prog} = 25$ and 40 $M_\odot$ and spherical explosion models. Middle panel: same as the top panel, but with the data from P. N. Thibodeaux et al. (2024). Bottom panel: same as the top panel, but with the data from Skúladóttir et al. (2024).

which is one of the end products of ^{22}Ne. For SNe exploding from a zero-metallicity star, the star does not begin with any observable amount of ^{14}N and ^{22}Ne; hence, its production of ^{55}Mn is naturally suppressed. The 1D model has a similar abundance pattern to the 25 $M_\odot$ model, where [Ca/Fe] and [Cr/Fe] are too high and [Mn/Fe] is too low, which prohibits the spherical model to be the full explanation of the VMP star.

In the bottom panel, we plot data points similar to those in the top panel but for the data set derived in Skúladóttir et al. (2024). The data set features a more conserved [Si/Fe], [Ti/Fe], and [Mn/Fe] compared to P. N. Thibodeaux et al. (2024), but some, such as [Sc/Fe] and [Co/Fe], are similar to that work. The 1D model predicts too high [Mg/Fe], [Si/Fe], [Ca/Fe], [Ti/Fe], and [Ni/Fe] as in previous comparisons. The 25 $M_\odot$ model also suffers from similar problems and fails to be the best-fit model, except that it has a more comparable [Ni/Fe] and [Zn/Fe] in that object. The 40 $M_\odot$ model is more compatible with LAMOST J1010+2358 owing to its lower [Mg/Fe], [Si/Fe], and Fe-group elements. Still, it predicts the [Ti/Fe] and [Zn/Fe] too high, while [Mn/Fe] is too low to be a satisfactory interpretation of this VMP star.

The object is extensively compared in Q.-F. Xing et al. (2023). The Chandrasekhar-mass white dwarf yields are used to compare with this VMP star. However, in such an early system, we expect that the contribution from the Chandrasekhar-mass white dwarf explosion is low because of the time delay from the formation of the white dwarf until it reaches the ignition mass (C. Kobayashi et al. 2020). In fact, the sub-Chandrasekhar-mass Type Ia SN yields in S.-C. Leung & K. Nomoto (2020) show low or subsolar [Ti/Fe], [Cr/Fe], [Mn/Fe], and [Co/Fe] in contrast to the Chandrasekhar-mass counterpart (see, e.g., K. Nomoto & S.-C. Leung 2017; K. Nomoto & S.-C. Leung 2018; S.-C. Leung & K. Nomoto 2018). The mixing of yields of jet-driven SNe with the low-metallicity sub-Chandrasekhar models can lead to lower mass fraction ratios in Ti and Cr.

Given the strong mass dependence of [Ne/O] as demonstrated in the previous section, the knowledge of spectral data from lines of these two elements will provide important insights for determining the origin of the SN (1D vs. 2D CCSN, PISN). In particular, a major disparity comes from the stringent constraints of [Ti/Fe] and [Cr/Fe], where our models tend to predict a high value, while LAMOST J1010+2358 has close-to-solar values. The production of Ti and Cr centered around matter with a temperature $\sim(4-5)\times10^9$ K and a density of about 10^6-10^7 g cm^{-3}. As shown in Figure 17, most jet-driven SN models tend to produce solar to even supersolar [Ti/Fe] and [V/Fe]. In Table 8 it becomes clear that different spectral modeling and input physics (e.g., non-LTE or not) could lead to distinctive interpretations of the chemical abundances. Future accurate and model-independent measurements of these objects will provide further hints on the shock heating history in the ejecta and the general progenitor mass of the VMP star.

6. Conclusion

In this paper, we compute nucleosynthesis yields of our jet-driven SN models using multidimensional simulations. We calculate explosions of massive stars from 20 to 40 $M_\odot$ and associated explosive nucleosynthesis. We study how the explosion hydrodynamics and nucleosynthesis depend on the progenitor properties (mass, mass cut, and dimensionality). We compare the ejecta observable, including chemical abundances with available metal-poor stars, SNe, and metal-poor galaxies. Some of our models are consistent with the recently observed EMP galaxies. Below we list our findings of this work:

1. The inner mass cut and the initial black hole mass strongly change the [Fe/O] ratio of the ejecta and the ejecta mass.
2. Asphericity of the explosion provides a reasonable energy budget to match the observed high velocity, and the thermodynamics history is distinct from the spherical counterpart.
3. The spread of the explosion energetics can explain the diversity of the observed SN ejecta mass and the ^{56}Ni distribution. Some parameter space featuring the extremely high ^{56}Ni mass ($>1\,M_{\odot}$) and high ejecta mass ($\sim 10\,M_{\odot}$) remains to be solved.
4. The lower-mass ($\sim 25\,M_{\odot}$) models can produce a Ti–V relation consistent with that from the metal-poor stars in the stellar survey in the literature.
5. The EMP galaxies can be characterized by their [Ne/O], which is sensitive to the progenitor mass. A high [Ne/O] corresponds to a lower progenitor mass and vice versa.
6. Despite the EMP nature, i.e., even without the contribution of Fe from Type Ia SNe, the abundance ratios [(Si, S, Ar, Ca, Fe)/O] of these EMP galaxies are as high as the solar values, which can be matched with single or a few jet-driven SN explosions.
7. In the energetic jet-driven SNe, despite that explosive O burning converts O to Si, S, A, and Ca, [(Si, S, Ar, Ca)/O] do not exceed the solar ratios. This is consistent with the observed ratios in EMP galaxies.
8. The VMP star J1010+2358 in the Galactic halo, poor in [Mg/Fe] and [Mn/Fe], can be well matched with our jet-driven SN of the 25 $M_{\odot}$ progenitor.
9. Metal-poor stars tend to exhibit the abundance pattern of a mixture of multiple SN explosions instead of a single one.

Acknowledgments

We thank Frank Timmes for the open-source subroutines of the Helmholtz equation of state and the torch nuclear reaction network. This material is based on work supported by the National Science Foundation under grant AST-2316807. K.N. acknowledges support by the World Premier International Research Center Initiative (WPI) and JSPS KAKENHI grant Nos. JP20K04024, JP21H04499, and JP23K03452.

Software: Numpy (C. R. Harris et al. 2020), Matplotlib (J. D. Hunter 2007), Pandas (The Pandas Development Team 2022).

Appendix A
Nucleosynthetic Yields of Jet-driven Supernova Models

In Section 2 we present in detail how the dynamics and nucleosynthesis yields depend on the dimension, jet energetics, and mass cut, and we focus on some key elements, including [Ne/O], [Si/O], [S/O], and [Fe/O], that are commonly observed in EMP galaxies. Here we present yields of other important elemental pairs for further comparison with available observation data. In Tables 10–13, we list the results for the for the model series of S20, S25a, S25b, and S25c, respectively.

Table 10
The Masses of Fe and ^{56}Ni of the Models in Series S20 and the Elemental Ratios [Z/O] of other Major Elements, Defined in Equation (1)

Model	M(Fe)	M(^{56}Ni)	[C/O]	[Mg/O]	[Ca/O]	[Ti/O]	[Cr/O]	[Mn/O]	[Co/O]	[Ni/O]	[Zn/O]
S20-0250-1000-15	0.038	0.035	−0.56	−0.15	−1.00	−0.48	−0.84	−1.80	−0.98	−0.71	−0.93
S20-0500-500-15	0.037	0.035	−0.61	−0.15	−0.82	−0.52	−0.75	−1.51	−0.89	−0.56	−1.16
S20-0500-1000-15	0.045	0.042	−0.62	−0.15	−0.71	−0.62	−0.64	−1.00	−0.80	−0.50	−1.15
S20-0500-2000-15	0.046	0.043	−0.63	−0.15	−0.69	−0.71	−0.78	−1.20	−0.78	−0.43	−1.12
S20-1000-0250-15	0.037	0.034	−0.63	−0.14	−0.93	−0.66	−0.85	−1.60	−1.01	−0.55	−1.22
S20-1000-0500-15	0.047	0.044	−0.64	−0.15	−0.55	−0.76	−0.74	−0.83	−0.80	−0.30	−1.21
S20-1000-1000-15	0.029	0.027	−0.64	−0.15	−0.61	−1.08	−0.88	−0.90	−0.87	−0.35	−1.88
S20-1000-2000-15	0.030	0.027	−0.65	−0.15	−0.56	−0.97	−0.84	−0.88	−0.87	−0.37	−2.00
S20-1000-4000-15	0.047	0.043	−0.65	−0.15	−0.54	−0.69	−0.70	−0.69	−0.73	−0.28	−1.67
S20-2000-0500-15	0.058	0.053	−0.65	−0.15	−0.41	−0.74	−0.67	−0.69	−0.57	−0.24	−1.12
S20-2000-1000-15	0.047	0.044	−0.66	−0.16	−0.43	−0.87	−0.73	−0.78	−0.64	−0.27	−1.54
S20-2000-2000-15	0.052	0.047	−0.67	−0.16	−0.27	−0.80	−0.68	−0.55	−0.42	−0.23	−1.46
S20-4000-1000-15	0.064	0.053	−0.66	−0.15	−0.23	−0.63	−0.38	−0.22	−0.48	−0.31	−1.65
S20-4000-2000-15	0.057	0.039	−0.66	−0.15	−0.33	−0.71	−0.30	−0.07	−0.35	−0.27	−1.69

Note. Masses are in units of solar mass. See also Tables 1–4 for M(O) and other elements of this model series.

Table 11
Same as Table 10, but for the Models in Series S25a

Model	M(Fe)	$M(^{56}\mathrm{Ni})$	[C/O]	[Mg/O]	[Ca/O]	[Ti/O]	[Cr/O]	[Mn/O]	[Co/O]	[Ni/O]	[Zn/O]
S25a-0250-1000-15	0.110	0.105	−0.25	−0.65	0.14	0.30	0.13	−1.17	−0.93	−0.13	−0.05
S25a-0250-2000-15	0.014	0.014	−0.22	−0.72	0.14	−0.54	−0.32	−1.63	−2.24	−1.84	−2.46
S25a-0500-0500-15	0.100	0.096	−0.26	−0.68	−0.17	0.02	−0.11	−1.53	−1.16	−0.56	−0.41
S25a-0500-1000-15	0.151	0.144	−0.34	−0.64	0.06	0.11	0.04	−1.36	−0.81	−0.42	−0.52
S25a-0500-2000-15	0.060	0.058	−0.33	−0.67	−0.01	−0.44	−0.23	−1.63	−1.40	−1.02	−0.51
S25a-0500-4000-15	0.167	0.160	−0.39	−0.60	0.04	−0.03	−0.04	−1.35	−0.68	−0.38	−0.61
S25a-1000-0250-15	0.042	0.040	−0.22	−0.68	−0.47	−0.01	−0.37	−1.93	−1.20	−0.56	−0.40
S25a-1000-0500-15	0.149	0.142	−0.43	−0.57	−0.02	−0.10	−0.12	−1.46	−0.75	−0.40	−0.85
S25a-1000-1000-15	0.206	0.197	−0.45	−0.54	0.07	−0.07	−0.01	−1.25	−0.53	−0.13	0.70
S25a-1000-1000-30	0.262	0.253	−0.47	−0.51	0.10	0.08	−0.03	−1.45	−0.25	0.20	1.28
S25a-1000-2000-15	0.213	0.204	−0.46	−0.52	0.04	−0.12	−0.06	−1.30	−0.55	−0.17	−0.62
S25a-1000-2000-30	0.353	0.341	−0.48	−0.51	0.15	0.11	0.00	−1.47	−1.05	−0.25	−0.10
S25a-1000-4000-15	0.056	0.054	−0.45	−0.50	−0.15	−0.63	−0.37	−0.92	−0.90	−0.76	−1.81
S25a-2000-0250-15	0.216	0.207	−0.47	−0.53	−0.11	−0.09	−0.09	−1.40	−0.68	−0.30	−0.54
S25a-2000-0500-15	0.247	0.236	−0.50	−0.49	0.04	−0.14	−0.06	−0.90	−0.41	−0.06	−0.64
S25a-2000-1000-15	0.235	0.225	−0.51	−0.48	0.02	−0.16	−0.10	−1.32	−0.50	−0.03	−0.63
S25a-2000-1000-30	0.367	0.352	−0.51	−0.48	0.15	0.27	0.10	−1.31	−0.67	−0.18	−0.14
S25a-2000-2000-15	0.198	0.184	−0.52	−0.47	0.02	−0.28	−0.17	−0.68	−0.09	0.30	0.94
S25a-2000-2000-30	0.427	0.410	−0.52	−0.50	0.21	0.17	0.10	−1.34	−0.55	−0.12	−0.24
S25a-4000-0500-15	0.280	0.269	−0.54	−0.44	0.14	−0.06	−0.03	−1.27	−0.52	−0.01	−0.57
S25a-4000-1000-15	0.252	0.242	−0.55	−0.46	0.25	−0.16	0.00	−0.91	−0.35	−0.00	−0.79
S25a-4000-2000-15	0.332	0.311	−0.54	−0.47	0.36	−0.11	0.12	−0.08	−0.09	0.21	−0.60

Note. See also Tables 1–4 for M(O) and other elements of this model series.

Table 12
Same as Table 10, but for the Models in Series S25b

Model	M(Fe)	$M(^{56}\mathrm{Ni})$	[C/O]	[Mg/O]	[Ca/O]	[Ti/O]	[Cr/O]	[Mn/O]	[Co/O]	[Ni/O]	[Zn/O]
S25b-0500-1000-15	0.080	0.077	−0.28	−0.65	0.09	0.18	0.10	−1.26	−0.72	−0.40	−0.54
S25b-0500-2000-15	0.024	0.023	−0.24	−0.71	0.03	−0.50	−0.24	−1.49	−1.67	−1.39	−1.83
S25b-1000-0500-15	0.058	0.056	−0.34	−0.62	−0.01	−0.34	−0.19	−1.56	−0.85	−0.69	−1.46
S25b-1000-1000-15	0.108	0.103	−0.39	−0.59	0.03	−0.11	−0.05	−1.53	−0.63	−0.38	−0.85
S25b-1000-2000-15	0.121	0.116	−0.40	−0.56	0.04	−0.16	−0.07	−1.29	−0.64	−0.18	−0.74
S25b-1000-4000-15	0.043	0.041	−0.44	−0.50	−0.14	−0.71	−0.50	−1.25	−0.90	−0.50	−1.96
S25b-2000-0500-15	0.132	0.127	−0.46	−0.52	0.02	−0.18	−0.09	−1.40	−0.57	−0.18	−0.95
S25b-2000-1000-15	0.139	0.134	−0.48	−0.51	0.05	−0.23	−0.10	−1.22	−0.52	−0.11	−0.96
S25b-2000-2000-15	0.143	0.137	−0.48	−0.49	−0.01	−0.30	−0.11	−0.85	−0.47	−0.09	−0.91
S25b-4000-1000-15	0.119	0.115	−0.51	−0.48	0.17	−0.34	−0.07	−1.42	−0.73	−0.44	−1.59
S25b-4000-2000-15	0.110	0.102	−0.52	−0.50	0.26	−0.34	−0.03	−0.29	−0.51	−0.19	−2.12

Note. See also Tables 1–4 for M(O) and other elements of this model series.

Table 13
Same as Table 10, but for the Models in Series S25c

Model	M(Fe)	$M(^{56}\mathrm{Ni})$	[C/O]	[Mg/O]	[Ca/O]	[Ti/O]	[Cr/O]	[Mn/O]	[Co/O]	[Ni/O]	[Zn/O]
S25c-0500-1000-15	0.070	0.067	−0.30	−0.61	−0.12	0.04	−0.04	−1.29	−0.62	−0.26	−0.59
S25c-0500-2000-15	0.062	0.060	−0.27	−0.67	0.07	−0.33	−0.20	−1.60	−0.84	−0.46	−1.07
S25c-1000-0500-15	0.083	0.080	−0.27	−0.65	0.03	−0.04	−0.00	−1.42	−0.62	−0.40	−0.84
S25c-1000-1000-15	0.078	0.074	−0.30	−0.65	−0.03	−0.31	−0.24	−1.36	−0.68	−0.29	−1.00
S25c-1000-2000-15	0.066	0.064	−0.36	−0.61	−0.10	−0.51	−0.36	−1.45	−0.92	−0.50	−1.16
S25c-1000-4000-15	0.059	0.057	−0.43	−0.53	−0.08	−0.67	−0.64	−1.44	−0.82	−0.45	−1.64
S25c-2000-0500-15	0.111	0.107	−0.38	−0.59	−0.02	−0.31	−0.19	−1.52	−0.83	−0.46	−1.04
S25c-2000-1000-15	0.120	0.114	−0.44	−0.55	0.00	−0.35	−0.20	−1.10	−0.57	−0.29	−1.08
S25c-2000-2000-15	0.143	0.138	−0.49	−0.51	0.05	−0.43	−0.25	−1.24	−0.58	−0.17	−1.20
S25c-4000-1000-15	0.076	0.074	−0.49	−0.51	0.02	−0.55	−0.26	−1.40	−1.03	−0.89	−2.29
S25c-4000-2000-15	0.127	0.122	−0.50	−0.50	0.12	−0.46	−0.14	−0.76	−0.72	−0.32	−1.48

Note. See also Tables 1–4 for M(O) and other elements of this model series.

Appendix B
Nucleosynthetic Yields of Spherical Models

In Section 2 we described how the mixing–fallback mechanism of the spherical explosion model can mimic the jet-driven SNe. Here we present the total nucleosynthetic yields of the massive-star explosions assuming spherical explosion of various masses (20, 25, and 40 $M_{\odot}$) and explosion energies (10^{51} and 10^{52} erg). The entire envelope is assumed to be ejected without mixing and fallback. In Tables 14–16 we list the nucleosynthetic yields of these explosion models.

Table 14
The Isotope Yields Table for Spherical Explosion Models

Isotope	$M = 20$, $E = 1$	$M = 25$, $E = 1$	$M = 40$, $E = 1$	$M = 20$, $E = 10$	$M = 25$, $E = 10$	$M = 40$, $E = 10$
^{12}C	2.12×10^{-1}	3.6×10^{-1}	4.33×10^{-1}	1.89×10^{-1}	2.73×10^{-1}	4.32×10^{-1}
^{13}C	2.34×10^{-9}	1.25×10^{-9}	1.32×10^{-9}	1.39×10^{-9}	6.99×10^{-8}	5.57×10^{-9}
^{14}N	3.10×10^{-7}	5.47×10^{-7}	9.45×10^{-8}	2.56×10^{-7}	1.61×10^{-6}	3.63×10^{-7}
^{15}N	7.5×10^{-7}	3.74×10^{-6}	9.48×10^{-6}	1.40×10^{-6}	4.62×10^{-6}	1.17×10^{-5}
^{16}O	2.15	2.84	8.24	2.02	2.26	7.50
^{17}O	5.19×10^{-8}	3.73×10^{-9}	1.54×10^{-9}	2.85×10^{-9}	1.8×10^{-8}	3.27×10^{-9}
^{18}O	5.77×10^{-11}	4.32×10^{-9}	5.31×10^{-12}	1.93×10^{-7}	2.96×10^{-8}	3.27×10^{-11}
^{19}F	1.89×10^{-10}	1.93×10^{-10}	8.97×10^{-11}	1.61×10^{-10}	6.15×10^{-10}	2.66×10^{-10}
^{20}Ne	9.19×10^{-1}	5.18×10^{-1}	3.11×10^{-1}	7.29×10^{-1}	2.53×10^{-1}	3.25×10^{-1}
^{21}Ne	3.35×10^{-7}	6.66×10^{-7}	3.19×10^{-7}	4.70×10^{-7}	1.32×10^{-5}	8.16×10^{-7}
^{22}Ne	4.38×10^{-7}	4.00×10^{-6}	7.10×10^{-8}	6.25×10^{-6}	5.71×10^{-6}	6.41×10^{-6}
^{23}Na	2.22×10^{-5}	2.90×10^{-5}	1.40×10^{-6}	3.56×10^{-5}	5.64×10^{-5}	5.65×10^{-6}
^{24}Mg	1.45×10^{-1}	1.10×10^{-1}	4.63×10^{-1}	1.39×10^{-1}	9.11×10^{-2}	3.89×10^{-1}
^{25}Mg	1.57×10^{-6}	2.26×10^{-6}	7.14×10^{-7}	5.14×10^{-6}	1.38×10^{-5}	2.91×10^{-6}
^{26}Mg	3.10×10^{-6}	1.20×10^{-5}	8.24×10^{-7}	2.30×10^{-5}	2.48×10^{-5}	1.53×10^{-5}
^{26}Al	4.66×10^{-28}	1.78×10^{-26}	9.52×10^{-28}	5.68×10^{-27}	1.75×10^{-26}	9.52×10^{-28}
^{27}Al	8.95×10^{-5}	1.79×10^{-4}	1.10×10^{-4}	2.20×10^{-4}	3.38×10^{-4}	1.76×10^{-4}
^{28}Si	9.20×10^{-2}	3.9×10^{-1}	9.21×10^{-1}	1.45×10^{-1}	4.15×10^{-1}	9.70×10^{-1}
^{29}Si	2.60×10^{-5}	6.23×10^{-5}	1.66×10^{-4}	8.17×10^{-5}	1.61×10^{-4}	2.6×10^{-4}
^{30}Si	2.69×10^{-5}	4.20×10^{-5}	4.20×10^{-5}	1.50×10^{-4}	2.18×10^{-4}	1.19×10^{-4}
^{31}P	3.84×10^{-5}	1.0×10^{-4}	1.27×10^{-4}	1.14×10^{-4}	1.85×10^{-4}	2.64×10^{-4}
^{32}S	5.67×10^{-2}	1.76×10^{-1}	4.85×10^{-1}	6.58×10^{-2}	2.32×10^{-1}	5.31×10^{-1}
^{33}S	3.57×10^{-5}	4.87×10^{-5}	5.9×10^{-5}	5.95×10^{-5}	9.19×10^{-5}	9.66×10^{-5}
^{34}S	2.50×10^{-5}	2.70×10^{-5}	9.90×10^{-6}	1.55×10^{-4}	2.77×10^{-4}	7.27×10^{-5}
^{36}S	1.82×10^{-11}	4.90×10^{-12}	4.51×10^{-12}	8.59×10^{-12}	7.50×10^{-12}	5.69×10^{-12}
^{35}Cl	1.56×10^{-5}	3.29×10^{-5}	5.52×10^{-5}	1.70×10^{-4}	1.80×10^{-4}	1.37×10^{-4}
^{37}Cl	2.20×10^{-5}	1.50×10^{-5}	6.42×10^{-6}	1.10×10^{-5}	1.30×10^{-5}	2.29×10^{-5}
^{36}Ar	1.26×10^{-2}	3.56×10^{-2}	9.83×10^{-2}	1.37×10^{-2}	5.15×10^{-2}	1.9×10^{-1}
^{38}Ar	1.3×10^{-5}	1.0×10^{-5}	2.66×10^{-6}	3.17×10^{-5}	5.78×10^{-5}	1.95×10^{-5}
^{40}Ar	2.36×10^{-14}	5.63×10^{-15}	8.58×10^{-15}	7.44×10^{-15}	4.66×10^{-15}	2.80×10^{-15}
^{39}K	1.53×10^{-5}	3.18×10^{-5}	2.86×10^{-5}	7.20×10^{-5}	1.30×10^{-4}	7.4×10^{-5}
^{40}K	3.60×10^{-11}	8.51×10^{-12}	9.61×10^{-12}	8.56×10^{-12}	4.48×10^{-12}	4.24×10^{-12}
^{41}K	9.89×10^{-6}	3.53×10^{-6}	1.68×10^{-6}	3.85×10^{-6}	1.55×10^{-6}	7.45×10^{-6}
^{40}Ca	1.12×10^{-2}	3.33×10^{-2}	1.00×10^{-1}	1.45×10^{-2}	5.55×10^{-2}	1.10×10^{-1}
^{42}Ca	1.46×10^{-6}	5.54×10^{-6}	2.46×10^{-7}	8.68×10^{-6}	1.61×10^{-5}	1.11×10^{-6}
^{43}Ca	2.45×10^{-6}	1.49×10^{-6}	7.60×10^{-7}	4.55×10^{-6}	5.15×10^{-6}	2.62×10^{-6}
^{44}Ca	3.74×10^{-5}	9.50×10^{-5}	3.12×10^{-4}	1.69×10^{-4}	4.76×10^{-4}	2.80×10^{-4}
^{46}Ca	1.57×10^{-18}	1.54×10^{-21}	8.52×10^{-24}	4.65×10^{-20}	8.51×10^{-22}	4.60×10^{-23}
^{48}Ca	1.32×10^{-24}	1.56×10^{-24}	2.55×10^{-24}	1.61×10^{-24}	2.30×10^{-24}	3.54×10^{-24}
^{45}Sc	1.49×10^{-6}	6.45×10^{-6}	6.38×10^{-8}	1.17×10^{-5}	8.84×10^{-6}	5.12×10^{-6}
^{46}Ti	1.00×10^{-6}	6.44×10^{-6}	8.6×10^{-9}	9.15×10^{-6}	2.85×10^{-5}	1.56×10^{-6}
^{47}Ti	2.98×10^{-6}	4.17×10^{-6}	9.74×10^{-7}	1.28×10^{-5}	2.16×10^{-5}	7.60×10^{-6}
^{48}Ti	1.75×10^{-4}	3.92×10^{-4}	1.54×10^{-3}	4.66×10^{-4}	1.47×10^{-3}	1.91×10^{-3}
^{49}Ti	2.54×10^{-6}	5.31×10^{-6}	1.5×10^{-6}	3.11×10^{-5}	1.39×10^{-5}	5.69×10^{-6}
^{50}Ti	7.50×10^{-17}	1.81×10^{-19}	6.93×10^{-22}	1.66×10^{-18}	2.69×10^{-21}	1.22×10^{-22}
^{50}V	1.67×10^{-13}	6.27×10^{-15}	3.64×10^{-15}	8.35×10^{-15}	1.56×10^{-16}	1.33×10^{-15}
^{51}V	3.89×10^{-5}	4.60×10^{-5}	1.84×10^{-5}	1.67×10^{-4}	3.85×10^{-4}	8.17×10^{-5}
^{50}Cr	1.15×10^{-5}	1.00×10^{-5}	6.77×10^{-7}	6.50×10^{-5}	1.80×10^{-4}	8.57×10^{-6}
^{52}Cr	2.24×10^{-3}	4.29×10^{-3}	1.62×10^{-2}	2.95×10^{-3}	1.12×10^{-2}	2.79×10^{-2}
^{53}Cr	3.30×10^{-5}	2.53×10^{-5}	1.26×10^{-4}	3.80×10^{-5}	4.25×10^{-5}	1.87×10^{-4}
^{54}Cr	1.20×10^{-12}	1.21×10^{-13}	1.67×10^{-14}	3.44×10^{-14}	1.99×10^{-15}	9.56×10^{-15}
^{55}Mn	6.20×10^{-5}	7.82×10^{-5}	1.10×10^{-4}	1.52×10^{-4}	3.80×10^{-4}	3.48×10^{-4}
^{54}Fe	1.67×10^{-5}	1.80×10^{-5}	2.88×10^{-5}	3.70×10^{-5}	5.27×10^{-5}	9.18×10^{-5}
^{56}Fe	1.49×10^{-1}	2.47×10^{-1}	5.80×10^{-1}	2.60×10^{-1}	7.97×10^{-1}	11.84×10^{-1}
^{57}Fe	1.58×10^{-3}	3.42×10^{-3}	7.32×10^{-3}	4.47×10^{-3}	1.31×10^{-2}	1.32×10^{-2}
^{58}Fe	4.16×10^{-13}	3.70×10^{-13}	5.84×10^{-13}	5.59×10^{-14}	1.77×10^{-13}	8.44×10^{-13}

Table 14
(Continued)

Isotope	$M = 20$, $E = 1$	$M = 25$, $E = 1$	$M = 40$, $E = 1$	$M = 20$, $E = 10$	$M = 25$, $E = 10$	$M = 40$, $E = 10$
^{60}Fe	1.93×10^{-24}	2.00×10^{-25}	2.87×10^{-25}	1.85×10^{-25}	2.73×10^{-25}	3.90×10^{-25}
^{59}Co	6.87×10^{-4}	2.60×10^{-4}	2.8×10^{-4}	2.37×10^{-3}	3.59×10^{-3}	6.46×10^{-4}
^{58}Ni	4.61×10^{-4}	3.68×10^{-4}	4.47×10^{-4}	1.89×10^{-3}	3.92×10^{-3}	1.38×10^{-3}
^{60}Ni	4.30×10^{-3}	7.62×10^{-3}	1.27×10^{-2}	8.96×10^{-3}	2.32×10^{-2}	2.48×10^{-2}
^{61}Ni	5.19×10^{-5}	1.17×10^{-4}	1.99×10^{-4}	1.80×10^{-4}	3.76×10^{-4}	3.78×10^{-4}
^{62}Ni	2.80×10^{-5}	5.48×10^{-5}	1.28×10^{-4}	1.95×10^{-4}	3.12×10^{-4}	1.90×10^{-4}
^{64}Ni	2.79×10^{-18}	9.67×10^{-17}	1.84×10^{-15}	6.42×10^{-18}	1.61×10^{-17}	3.19×10^{-16}
^{63}Cu	2.10×10^{-5}	6.6×10^{-6}	1.00×10^{-6}	1.82×10^{-4}	1.00×10^{-4}	2.28×10^{-5}
^{65}Cu	9.88×10^{-7}	2.79×10^{-6}	8.56×10^{-6}	3.80×10^{-6}	8.95×10^{-6}	1.20×10^{-5}
^{64}Zn	2.35×10^{-4}	3.58×10^{-4}	7.10×10^{-4}	7.70×10^{-4}	1.82×10^{-3}	1.90×10^{-3}
^{66}Zn	2.79×10^{-6}	5.50×10^{-6}	1.79×10^{-5}	1.87×10^{-5}	4.8×10^{-5}	2.22×10^{-5}
^{67}Zn	4.58×10^{-7}	1.96×10^{-7}	1.44×10^{-8}	1.38×10^{-6}	7.98×10^{-7}	1.48×10^{-6}
^{68}Zn	2.43×10^{-6}	5.50×10^{-6}	8.20×10^{-6}	4.90×10^{-6}	1.16×10^{-5}	1.19×10^{-5}
^{70}Zn	1.21×10^{-26}	2.73×10^{-26}	3.53×10^{-25}	1.47×10^{-26}	3.98×10^{-26}	1.16×10^{-25}

Note. Masses are in units of $M_{\odot}$, and energies are in units of 10^{51} erg.

Table 15
Same as Table 14, but for Short-lived Radioactive Isotopes

Isotope	$M = 20$, $E = 1$	$M = 25$, $E = 1$	$M = 40$, $E = 1$	$M = 20$, $E = 10$	$M = 25$, $E = 10$	$M = 40$, $E = 10$
^{22}Na	4.40×10^{-7}	7.56×10^{-7}	6.50×10^{-8}	3.99×10^{-7}	9.42×10^{-7}	1.37×10^{-7}
^{26}Al	2.79×10^{-6}	3.33×10^{-6}	8.25×10^{-7}	5.34×10^{-6}	6.55×10^{-6}	1.90×10^{-6}
^{39}Ar	8.79×10^{-13}	6.90×10^{-14}	7.90×10^{-14}	3.40×10^{-13}	1.55×10^{-13}	6.46×10^{-14}
^{40}K	3.80×10^{-11}	8.55×10^{-12}	9.66×10^{-12}	8.61×10^{-12}	4.51×10^{-12}	4.26×10^{-12}
^{41}Ca	8.42×10^{-6}	3.27×10^{-6}	1.46×10^{-6}	1.52×10^{-6}	1.14×10^{-6}	4.82×10^{-6}
^{44}Ti	3.61×10^{-5}	8.20×10^{-5}	3.14×10^{-4}	1.67×10^{-4}	4.26×10^{-4}	2.85×10^{-4}
^{48}V	2.23×10^{-7}	3.16×10^{-8}	2.68×10^{-7}	2.47×10^{-9}	1.54×10^{-8}	1.20×10^{-7}
^{49}V	1.91×10^{-7}	1.30×10^{-9}	4.35×10^{-9}	5.41×10^{-9}	1.18×10^{-9}	2.68×10^{-9}
^{53}Mn	1.14×10^{-5}	2.36×10^{-7}	3.52×10^{-6}	3.48×10^{-8}	8.13×10^{-8}	1.33×10^{-6}
^{60}Fe	2.67×10^{-23}	5.16×10^{-26}	1.85×10^{-25}	6.65×10^{-26}	4.14×10^{-26}	1.29×10^{-25}
^{56}Co	2.42×10^{-5}	2.85×10^{-6}	1.88×10^{-5}	1.86×10^{-7}	1.22×10^{-6}	1.19×10^{-5}
^{57}Co	1.60×10^{-6}	1.32×10^{-7}	5.55×10^{-7}	2.62×10^{-8}	1.0×10^{-7}	4.64×10^{-7}
^{60}Co	1.89×10^{-18}	6.87×10^{-20}	8.19×10^{-20}	2.85×10^{-19}	1.51×10^{-20}	5.85×10^{-20}
^{56}Ni	1.49×10^{-1}	2.47×10^{-1}	5.80×10^{-1}	2.60×10^{-1}	7.97×10^{-1}	11.84×10^{-1}
^{57}Ni	1.58×10^{-3}	3.41×10^{-3}	7.33×10^{-3}	4.45×10^{-3}	1.30×10^{-2}	1.33×10^{-2}
^{59}Ni	5.54×10^{-4}	9.28×10^{-6}	1.71×10^{-5}	2.89×10^{-5}	3.34×10^{-5}	3.31×10^{-5}
^{63}Ni	2.70×10^{-19}	4.81×10^{-19}	2.42×10^{-18}	8.6×10^{-20}	1.54×10^{-19}	1.53×10^{-18}

Table 16
Same as Table 14, but for the Elemental Yields

Isotope	$M = 20$, $E = 1$	$M = 25$, $E = 1$	$M = 40$, $E = 1$	$M = 20$, $E = 10$	$M = 25$, $E = 10$	$M = 40$, $E = 10$
C	2.12×10^{-1}	3.6×10^{-1}	4.33×10^{-1}	1.89×10^{-1}	2.73×10^{-1}	4.32×10^{-1}
N	1.10×10^{-6}	4.29×10^{-6}	9.57×10^{-6}	1.29×10^{-6}	6.23×10^{-6}	1.21×10^{-5}
O	2.15	2.84	8.24	2.02	2.26	7.50
F	1.89×10^{-10}	1.93×10^{-10}	8.97×10^{-11}	1.61×10^{-10}	6.15×10^{-10}	2.66×10^{-10}
Ne	9.19×10^{-1}	5.18×10^{-1}	3.11×10^{-1}	7.29×10^{-1}	2.53×10^{-1}	3.25×10^{-1}
Na	2.22×10^{-5}	2.90×10^{-5}	1.40×10^{-6}	3.56×10^{-5}	5.64×10^{-5}	5.65×10^{-6}
Mg	1.45×10^{-1}	1.10×10^{-1}	4.63×10^{-1}	1.39×10^{-1}	9.12×10^{-2}	3.89×10^{-1}
Al	8.95×10^{-5}	1.79×10^{-4}	1.10×10^{-4}	2.20×10^{-4}	3.38×10^{-4}	1.76×10^{-4}
Si	9.20×10^{-2}	3.90×10^{-1}	9.22×10^{-1}	1.46×10^{-1}	4.15×10^{-1}	9.71×10^{-1}
P	3.84×10^{-5}	1.00×10^{-4}	1.27×10^{-4}	1.14×10^{-4}	1.85×10^{-4}	2.64×10^{-4}
S	5.68×10^{-2}	1.76×10^{-1}	4.85×10^{-1}	6.60×10^{-2}	2.32×10^{-1}	5.31×10^{-1}
Cl	3.77×10^{-5}	4.35×10^{-5}	6.17×10^{-5}	1.17×10^{-4}	1.93×10^{-4}	1.60×10^{-4}
Ar	1.26×10^{-2}	3.56×10^{-2}	9.83×10^{-2}	1.38×10^{-2}	5.16×10^{-2}	1.90×10^{-1}
K	2.52×10^{-5}	3.53×10^{-5}	3.3×10^{-5}	7.59×10^{-5}	1.31×10^{-4}	7.79×10^{-5}
Ca	1.13×10^{-2}	3.34×10^{-2}	1.0×10^{-1}	1.47×10^{-2}	5.60×10^{-2}	1.11×10^{-1}
Sc	1.49×10^{-6}	6.45×10^{-6}	6.38×10^{-8}	1.17×10^{-5}	8.84×10^{-6}	5.12×10^{-6}

Table 16
(Continued)

Isotope	$M = 20$, $E = 1$	$M = 25$, $E = 1$	$M = 40$, $E = 1$	$M = 20$, $E = 10$	$M = 25$, $E = 10$	$M = 40$, $E = 10$
Ti	1.81×10^{-4}	4.80×10^{-4}	1.54×10^{-3}	5.19×10^{-4}	1.53×10^{-3}	1.93×10^{-3}
V	3.89×10^{-5}	4.60×10^{-5}	1.84×10^{-5}	1.67×10^{-4}	3.85×10^{-4}	8.17×10^{-5}
Cr	2.28×10^{-3}	4.32×10^{-3}	1.64×10^{-2}	3.50×10^{-3}	1.13×10^{-2}	2.81×10^{-2}
Mn	6.20×10^{-5}	7.82×10^{-5}	1.10×10^{-4}	1.52×10^{-4}	3.80×10^{-4}	3.48×10^{-4}
Fe	1.51×10^{-1}	2.51×10^{-1}	5.87×10^{-1}	2.64×10^{-1}	8.10×10^{-1}	11.97×10^{-1}
Co	6.87×10^{-4}	2.60×10^{-4}	2.80×10^{-4}	2.37×10^{-3}	3.59×10^{-3}	6.46×10^{-4}
Ni	4.84×10^{-3}	8.16×10^{-3}	1.35×10^{-2}	1.11×10^{-2}	2.79×10^{-2}	2.68×10^{-2}
Cu	2.20×10^{-5}	8.85×10^{-6}	9.56×10^{-6}	1.85×10^{-4}	1.90×10^{-4}	3.31×10^{-5}
Zn	2.41×10^{-4}	3.69×10^{-4}	7.36×10^{-4}	7.94×10^{-4}	1.87×10^{-3}	1.12×10^{-3}

ORCID iDs

Shing-Chi Leung https://orcid.org/0000-0002-4972-3803
Ken'ichi Nomoto https://orcid.org/0000-0001-9553-0685

References

Arcones, A., & Thielemann, F.-K. 2023, A&ARv, 31, 1
Arnett, D., Fryxell, B., & Mueller, E. 1989, ApJL, 341, L63
Burrows, A., Dolence, J. C., & Murphy, J. W. 2012, ApJ, 759, 5
Burrows, A., & Vartanyan, D. 2021, Natur, 589, 29
Burrows, A., Vartanyan, D., Dolence, J. C., Skinner, M. A., & Radice, D. 2018, SSRv, 214, 33
Chené, A.-N., Mao, S., Lundquist, M., et al. 2021, AJ, 161, 109
Couch, S. M., Pooley, D., Wheeler, J. C., & Milosavljević, M. 2011, ApJ, 727, 104
Couch, S. M., Wheeler, J. C., & Milosavljević, M. 2009, ApJ, 696, 953
Cui, X.-Q., Zhao, Y.-H., Chu, Y.-Q., et al. 2012, RAA, 12, 1197
De Cia, A., Gal-Yam, A., Rubin, A., et al. 2018, ApJ, 860, 100
Dessart, L., Hillier, D. J., Yoon, S.-C., Waldman, R., & Livne, E. 2017, A&A, 603, A51
Ekström, S., Meynet, G., Chiappini, C., Hirschi, R., & Maeder, A. 2008, A&A, 489, 685
Ezzeddine, R., Frebel, A., Roederer, I. U., et al. 2019, ApJ, 876, 97
Fesen, R. A. 2001, ApJS, 133, 161
Foglizzo, T., Kazeroni, R., Guilet, J., et al. 2015, PASA, 32, e009
Fujimoto, S.-i., Kotake, K., Yamada, S., Hashimoto, M.-a., & Sato, K. 2006, ApJ, 644, 1040
Gomez, S., Berger, E., Nicholl, M., Blanchard, P. K., & Hosseinzadeh, G. 2022, ApJ, 941, 107
Hachisu, I., Matsuda, T., Nomoto, K., & Shigeyama, T. 1990, ApJL, 358, L57
Harris, C. R., Millman, K. J., van der Walt, S. J., et al. 2020, Natur, 585, 357
Hartwig, T., Yoshida, N., Magg, M., et al. 2018, MNRAS, 478, 1795
Heger, A., & Woosley, S. E. 2002, ApJ, 567, 532
Hirano, S., Hosokawa, T., Yoshida, N., Omukai, K., & Yorke, H. W. 2015, MNRAS, 448, 568
Höflich, P., Wheeler, J. C., & Wang, L. 1999, ApJ, 521, 179
Hunter, J. D. 2007, CSE, 9, 90
Ishigaki, M. N., Tominaga, N., Kobayashi, C., & Nomoto, K. 2018, ApJ, 857, 46
Isobe, Y., Ouchi, M., Suzuki, A., et al. 2022, ApJ, 925, 111
Iwamoto, K., Mazzali, P. A., Nomoto, K., et al. 1998, Natur, 395, 672
Iwamoto, N., Umeda, H., Tominaga, N., Nomoto, K., & Maeda, K. 2005, Sci, 309, 451
Izotov, Y. I., Thuan, T. X., Guseva, N. G., & Liss, S. E. 2018, MNRAS, 473, 1956
Janka, H.-T., Melson, T., & Summa, A. 2016, ARNPS, 66, 341
Jeong, M., Lee, Y. S., Beers, T. C., et al. 2023, ApJ, 948, 38
Khokhlov, A. M., Höflich, P. A., Oran, E. S., et al. 1999, ApJL, 524, L107
Kobayashi, C., Leung, S.-C., & Nomoto, K. 2020, ApJ, 895, 138
Kojima, T., Ouchi, M., Rauch, M., et al. 2020, ApJ, 898, 142
Kuroda, T., Arcones, A., Takiwaki, T., & Kotake, K. 2020, ApJ, 896, 102
Latif, M. A., Whalen, D., & Khochfar, S. 2022, ApJ, 925, 28
LeBlanc, J. M., & Wilson, J. R. 1970, ApJ, 161, 541
Lentz, E. J., Bruenn, S. W., Hix, W. R., et al. 2015, ApJL, 807, L31
Leung, S.-C., Chu, M.-C., & Lin, L.-M. 2015, MNRAS, 454, 1238
Leung, S.-C., & Nomoto, K. 2018, ApJ, 861, 143
Leung, S.-C., & Nomoto, K. 2020, ApJ, 888, 80
Leung, S.-C., & Nomoto, K. 2023, in The Sixteenth Marcel Grossmann Meeting. On Recent Developments in Theoretical and Experimental General Relativity, ed. R. Ruffini & G. Vereshchagin (Singapore: World Scientific Publishing), 4427
Leung, S.-C., Nomoto, K., & Suzuki, T. 2023, ApJ, 948, 80
MacFadyen, A. I., Woosley, S. E., & Heger, A. 2001, ApJ, 550, 410
Maeda, K., Mazzali, P. A., & Nomoto, K. 2006, ApJ, 645, 1331
Maeda, K., Nakamura, T., Nomoto, K., et al. 2002, ApJ, 565, 405
Mao, J., Zhou, P., Simionescu, A., et al. 2021, ApJL, 918, L17
Marigo, P., Girardi, L., Chiosi, C., & Wood, P. R. 2001, A&A, 371, 152
Martinet, S., Meynet, G., Ekström, S., Georgy, C., & Hirschi, R. 2023, A&A, 679, A137
Mazzali, P. A., Kawabata, K. S., Maeda, K., et al. 2005, Sci, 308, 1284
Mazzali, P. A., Nomoto, K., Patat, F., & Maeda, K. 2001, ApJ, 559, 1047
Melson, T., Janka, H.-T., Bollig, R., et al. 2015, ApJL, 808, L42
Mösta, P., Richers, S., Ott, C. D., et al. 2014, ApJL, 785, L29
Müller, B. 2020, LRCA, 6, 3
Müller, B. 2024, in from New Frontiers in GRMHD Simulations, ed. C. Bambi, Y. Mizuno, S. Shashank, & F. Yuan (Singapore: Springer)
Murphy, L. J., Groh, J. H., Ekström, S., et al. 2021, MNRAS, 501, 2745
Nagataki, S., Hashimoto, M.-a., Sato, K., & Yamada, S. 1997, ApJ, 486, 1026
Nagataki, S., Shimizu, T. M., & Sato, K. 1998, ApJ, 495, 413
Nakamura, T., Mazzali, P. A., Nomoto, K., & Iwamoto, K. 2001, ApJ, 550, 991
Nomoto, K., Kobayashi, C., & Tominaga, N. 2013, ARA&A, 51, 457
Nomoto, K., & Leung, S.-C. 2017, in Handbook of Supernovae, ed. A. W. Alsabti & P. Murdin (Cham: Springer Verlag AG), 1275
Nomoto, K., & Leung, S.-C. 2018, SSRv, 214, 67
Nomoto, K., Maeda, K., Umeda, H., et al. 2003, in A Massive Star Odyssey: From Main Sequence to Supernova, ed. K. van der Hucht, A. Herrero, & C. Esteban, 212 (San Francisco: Astronomical Society of the Pacific), 395
Obergaulinger, M., Cerdá-Durán, P., Müller, E., & Aloy, M. A. 2009, A&A, 498, 241
Obergaulinger, M., & Reichert, M. 2023, Nucleosynthesis in jet-driven and jet-associated supernovae, Handbook of Nuclear Physics (Singapore: Springer), 38
The Pandas Development Team 2022, pandas-dev/pandas: Pandas, v1.5.2, Zenodo, doi:10.5281/zenodo.7344967
Roederer, I. U., Preston, G. W., Thompson, I. B., et al. 2014, AJ, 147, 136
Seitenzahl, I. R., Ropke, F. K., Fink, M., & Pakmor, R. 2010, MNRAS, 407, 2297
Skúladóttir, Á., Koutsouridou, I., Vanni, I., et al. 2024, ApJL, 968, L23
Sneden, C., Cowan, J. J., Kobayashi, C., et al. 2016, ApJ, 817, 53
Song, H., Meynet, G., Li, Z., et al. 2020, ApJ, 892, 41
Strom, R., Johnston, H. M., Verbunt, F., & Aschenbach, B. 1995, Natur, 373, 590
Sukhbold, T., Ertl, T., Woosley, S. E., Brown, J. M., & Janka, H. T. 2016, ApJ, 821, 38
Surman, R., & McLaughlin, G. C. 2004, ApJ, 603, 611
Taddia, F., Sollerman, J., Fremling, C., et al. 2019, A&A, 621, A71
Thibodeaux, P. N., Ji, A. P., Cerny, W., Kirby, E. N., & Simon, J. D. 2024, arXiv:2404.17078
Thielemann, F.-K. 2019, in Nuclei in the Cosmos XV, 219, ed. A. Formicola et al. (Switzerland: Springer Nature AG), 125
Timmes, F. X. 1999, ApJS, 124, 241
Timmes, F. X., & Arnett, D. 1999, ApJS, 125, 277
Timmes, F. X., Hoffman, R. D., & Woosley, S. E. 2000, ApJS, 129, 377

Timmes, F. X., & Swesty, F. D. 2000, ApJS, 126, 501
Tominaga, N. 2009, ApJ, 690, 526
Tominaga, N., Maeda, K., Umeda, H., et al. 2007a, ApJL, 657, L77
Tominaga, N., Umeda, H., & Nomoto, K. 2007b, ApJ, 660, 516
Tran, H. D., Filippenko, A. V., Schmidt, G. D., et al. 1997, PASP, 109, 489
Travaglio, C., Hillebrandt, W., Reinecke, M., & Thielemann, F. K. 2004, A&A, 425, 1029
Umeda, H., & Nagele, C. 2024, ApJ, 961, 146
Umeda, H., & Nomoto, K. 2002, ApJ, 565, 385
Wang, L., & Mazzali, P. A. 1992, Natur, 355, 58
Watanabe, K., Ouchi, M., Nakajima, K., et al. 2024, ApJ, 962, 50
Weaver, T. A., Zimmerman, G. B., & Woosley, S. E. 1978, ApJ, 225, 1021
Woods, T. E., Heger, A., & Haemmerlé, L. 2020, MNRAS, 494, 2236
Woosley, S. E., & Weaver, T. A. 1995, ApJS, 101, 181
Xing, Q.-F., Gang, Z., Liu, Z.-W., et al. 2023, Natur, 1
York, D. G., Adelman, J., Anderson, J. E. J., et al. 2000, AJ, 120, 1579
Zhao, G., Chen, Y.-Q., Shi, J.-R., et al. 2006, ChJAA, 6, 265
Zhao, G., Zhao, Y.-H., Chu, Y.-Q., Jing, Y.-P., & Deng, L.-C. 2012, RAA, 12, 723